Robust omniphobic ceramic hollow fibre membrane with leaf-like copper oxide hierarchical structure by membrane distillation

Najib Meftah Almukhtar Omar [a,b], Mohd Hafiz Dzarfan Othman [a,*], Zhong Sheng Tai [a],
Ahmed Omar Aswaye Amhamed [b], Erna Yuliwati [c], Mohd Hafiz Puteh [a],
Tonni Agustiono Kurniawan [d], Mukhlis A. Rahman [a], Juhana Jaafar [a], Ahmad Fauzi Ismail [a]

[a] Advanced Membrane Technology Research Centre (AMTEC), Faculty of Chemical and Energy Engineering (FCEE), Universiti Teknologi Malaysia, 81310 UTM Skudai, Johor, Malaysia
[b] Chemical Engineering Department, Sabratha Faculty of Engineering, Sabratha University, Libya
[c] Program Study of Chemical Engineering, Faculty of Engineering, Universitas Muhammadiyah Palembang, Jalan A.Yani 13 Ulu Kota, Palembang 30263, Indonesia
[d] College of Ecology and the Environment, Xiamen University, Xiamen, 361102, Fujian, PR China

HIGHLIGHTS

- Robust omniphobic mullite-SS HFM with leaf-like surface structure
- High water contact angle by omniphobic mullite-SS HFM of up to 167°
- High permeate flux through the DCMD system to about 29 kg/m^2·h for 24 h operation
- High rejection performance of about 99.99 %

GRAPHICAL ABSTRACT
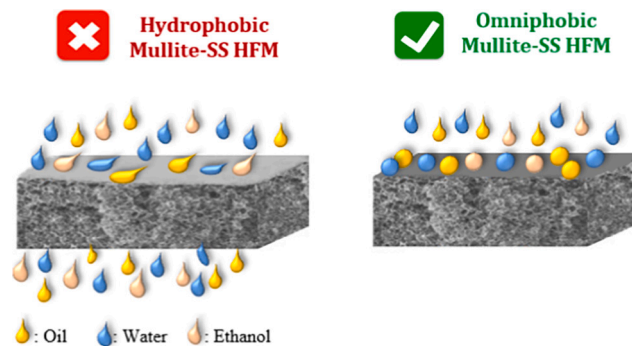
ABSTRACT

Omniphobic membranes have recently shown promising performance in water desalination using MD due to their ability to *repel all liquid drop types* and keep the membrane surface dry. This study successfully modified the surface of robust hydrophilic mullite-stainless steel hollow fibre membranes (M-SS HFMs) to omniphobic properties. The omniphobic layer was achieved through surface grafting with copper oxide (CuO) rough layer by a hydrothermal technique at different hydrothermal reaction times of 1, 2, 3, 4 and 5 h, followed by fluorination step using 1H,1H,2H,2H-perfluorode-cyltriethoxysilane (C8, 97 %). Next, the omniphobic membranes were characterized in terms of membrane morphology, roughness, mechanical strength, pore size/distribution, liquid entry pressure, contact angle and fouling accumulation. The prepared omniphobic M-SS HFMs were also tested through the DCMD system at 80 °C using a feed solution containing 35 g/L of NaCl and 10 mg/L of humic acid as a foulant agent. The results indicated that M-SS HFMs subjected to a 4 h hydrothermal reaction time, resulting in a leaf-like surface structure, exhibited superior characteristics compared to other omniphobic HFMs reported in the literature that used titania (SiO$_2$), zinc oxide (ZnO), and cobalt (Co$_3$O$_4$) as roughing material. These superior

* Corresponding author.
  E-mail address: hafiz@petroleum.utm.my (M.H.D. Othman).

features included higher roughness of 0.798 μm, liquid entry pressure of 5.40 bar, and enhanced liquid repellence and contact angles towards DI water of 167°, olive oil of 152°, and ethanol of 145°. Additionally, the M-SS HFMs at 4 h hydrothermal demonstrated remarkable performance in terms of rejection performance (99.99 %) and vapour flux stability of about 29 kg/m^2.h in DCMD operations, surpassing the performance of omniphobic HFMs fabricated using mullite-ball clay, mullite-kaolinite, and alumina (Al$_2$O$_3$). Notably, no fouling/wetting on the membrane surface and elements leaching was observed throughout the MD operation. These findings highlight the potential of this omniphobic HFM for seawater desalination using DCMD systems, even in the presence of organic contaminants.

1. Introduction

Hydrophobic ceramic membranes have several limitations in stability during long-term operation. Although they have a good slide-drop property on the membrane surface, they are easily fouled and wetted by low surface tension materials such as surfactants and organic substances in the feed solution [1–3]. This results in decreased performance of ceramic membranes and a reduced desalination efficiency due to fouling buildup on the membrane surface [3–5]. To address these challenges, developing new ceramic membranes with high anti-fouling/antiwetting resistance and stability is crucial for desalination applications [6]. In recent years, researchers have intensified efforts to overcome the drawbacks associated with hydrophobic surfaces by developing new superhydrophobic surfaces inspired by the self-cleaning features of animal feathers, and lotus leaves surfaces to mitigate the drawbacks of hydrophobic surface issues [3,5]. These superhydrophobic surfaces have been attributed to the repellant of all water drops on the surfaces of the membranes with high water contact angles of up to 150° and sliding angles lower than 10° [7–9]. On the other hand, they are vulnerable to fouling/wetting by low-surface tension materials such as alcohol, oils, and organic acids [10,11].

Considering the weak resistance of superhydrophobic surfaces to low-surface tension materials, omniphobic surfaces have been suggested as an effective solution to overcome this critical issue. Omniphobic ceramic membranes are advanced techniques with unique properties, such as high stability and resistance to organic and inorganic substances [3,12]. These membranes are highly efficient for separating liquids based on their hydrophobic and oleophobic properties, resisting water and oil drops [13]. They offer several benefits compared to traditional separation approaches, such as improved durability, better resistance to harsh chemical environments, and enhanced separation performance. These features make them a suitable choice for water treatment, chemical processing, and oil/gas separation applications [3,14]. Omniphobic surfaces are typically prepared by a re-entrant hierarchical structure with ultra-low surface energy to introduce no absorption to all liquid drops in feed solution and provide a strong repellent for water and low surface tension materials [15–17]. The re-entrant hierarchical structures are usually prepared using nanoparticle materials and are much-favoured for omniphobic surfaces due to their air pockets formation produced owing to surface roughness, which results in a steady Cassie-Bexter regime with a water contact angle higher than 150° [7,18]. The reduction of the membrane surface energy is usually performed by a fluorination process using a fluorination agent such as fluoroalkylsilane to reduce the adhesion force between liquid drops and the membrane surface [3,19].

Few nanoparticle materials such as Zinc oxide (ZnO), titanium dioxide (TiO$_2$), silica (SiO$_2$) and cobalt oxide (Co$_3$O$_4$) have been reported for preparing the omniphobic layer on the CHFMs in the literature [7,20,21]. Overall, these materials have advantages and disadvantages in omniphobic CHFMs fabrication. ZnO nanoparticles exhibit excellent hydrophobic and oleophobic properties, repelling water and oils effectively while minimizing fouling due to their low surface energy [22]. They also possess antimicrobial characteristics, inhibiting bacterial and fungal growth on the membrane [9]. However, caution is required as high concentrations of ZnO can have cytotoxic effects, necessitating

careful optimization of nanoparticle concentration for desired membrane performance and minimal environmental risks. TiO$_2$ nanoparticles are widely used for their photocatalytic properties, enabling self-cleaning capabilities under UV light [23–25]. While this enhances long-term stability and prevents fouling, careful control of nanoparticle loading is necessary to balance self-cleaning properties with membrane permeability [7]. The Co$_3$O$_4$ nanoparticles offer excellent catalytic activity for organic contaminant degradation, particularly useful in wastewater treatment [26]. However, considering potential drawbacks such as nanoparticle aggregation, precise optimization of Co$_3$O$_4$ nanoparticle concentration and dispersion is essential to maintain desired membrane properties without compromising integrity [21]. The SiO$_2$ nanoparticles offer a high surface area, enhancing reactivity and adsorption capacity [27]. Their stability and resistance to heat make them suitable for high-temperature processes and membrane surface grafting [20,28]. However, attention should be exercised because of the potential toxicity risks associated with prolonged exposure to high concentrations. In addition, their tendency to aggregate can hinder dispersion and impact their performance in water treatment applications involving membranes [29]. The omniphobic CHFMs prepared by these materials have only been applied for seawater desalination. Recently, graphene oxide (GO) has gained attention as a potential solution for treating industrial wastewater with complex contaminants, aiming to overcome the limitations of current hydrophobic membranes in MD processes [30,31]. Although GO has shown promise in wastewater treatment, it is crucial to acknowledge its drawbacks. One concern is the tendency of GO membranes to swell when exposed to water, which compromises their performance and structural stability. Additionally, fouling poses a challenge for GO membranes due to the presence of functional groups that facilitate the adsorption of organic and inorganic compounds [32].

In a study by Alfteesi et al. [20], silica sand CHFM was modified to achieve superomniphobic properties, with high contact angles observed for water (167°), palm oil (157°), and ethanol (146.1°), along with a salt rejection rate of 100 %. Li et al. [28] developed omniphobic PVDF composite membranes by coating SiO$_2$ nanoparticles via electrostatic adsorption and fluorination for effective wastewater treatment using DCMD. These membranes exhibited high contact angles exceeding 150° for water, diiodomethane, and ethylene glycol on the membrane surface. Abd Aziz et al. [7] improved the omniphobicity of mullite-ball clay HFM by incorporating organosilane-functionalized TiO$_2$ micro-flowers and nanorod layer deposition in DCMD desalination, resulting in excellent separation performance and superomniphobic properties against ethylene glycol (150°) and olive oil (140°). Similarly, Chen et al. [33] achieved remarkable separation performance and specific water contact angles using omniphobic ceramic membranes with zinc oxide nanoparticles and Al$_2$O$_3$ in DCMD. Lastly, Twibi et al. [21] introduced a novel approach for surface functionalization of mullite-kaolinite HFM by depositing organosilane-functionalized Co$_3$O$_4$ spider web-like layers, which exhibited superior salt separation performance and superomniphobic properties against water (165°), olive oil (142°), and engine oil (154°) in DCMD desalination.

Based on the principles of omniphobic surface construction, omniphobic membranes have been successfully synthesized with varied techniques. According to Omar et al. [3], the membrane surface

modification to omniphobic properties can be achieved by several techniques, including laser processing, chemical vapour deposition, sol-gel, chemical etching, spray and hydrothermal. Laser processing offers precise control and customization of surface properties, but it presents several limitations. These include high costs, time-consuming procedures, challenges in scalability, and the potential for heat damage or alteration of the substrate [34]. On the other hand, chemical vapour deposition (CVD) enables the growth of uniform thin films. However, its complexity and expense arise from the need for high temperatures and specific gas requirements. CVD may also introduce residual stress and defects, negatively impacting the durability and performance of the omniphobic layer [35]. The sol-gel method provides versatility in film creation but is associated with drawbacks such as time-consuming steps, hazardous chemicals, and safety concerns [36]. Spray coating for omniphobic layer preparation also has drawbacks, including challenges in achieving uniform coating thickness, resulting in performance variations. It may also lead to overspray and uneven distribution, causing inconsistencies in surface properties. Additionally, the durability of the sprayed layer can be compromised over time, particularly in high-stress or abrasive environments [37]. Finally, chemical etching, a widely used surface modification technique, has limitations, including material restrictions, uneven etching, surface roughness, and difficulties in achieving uniformity across large areas [38].

Among all reported techniques, hydrothermal has recently received more interest in creating roughness on the membrane surface by nanomaterials due to its significant attributions, such as simple handling, easy controlling, and low cost. By changing the reaction concentration, time, precursor, and ionic additive quantity, the membrane surface appearance and structure of the dispersed omniphobic layer on the membrane surface can be easily controlled [3,26]. The hydrothermal technique can efficiently construct the hierarchical structure of copper oxide (CuO) micro/nanoparticles by the direct growth of CuO particles on the membrane surface due to its ability to enhance particles adhesion and build up these particles with different morphologies and structures, such as flowers-like, nanorods-like and leaf-like structures on the membrane surface [39,40] as reported in many previous works [41–44]. Despite the unique properties and structures of CuO and its broad use to synthesize omniphobic surfaces with adequate structural stability in many applications. However, its use as a surface activator material to create hierarchical structures for surface modification of ceramic membranes to omniphobic properties for desalination processes has not been reported yet [8,45].

Membrane distillation is an innovative and promising process that offers efficient and energy-saving solutions for treating hypersaline water [3]. Notably, recent studies by Subrahmanya et al. [6,46] have made significant contributions to enhancing the performance of this process. In their studies, they have developed cutting-edge techniques such as self-heated systems and flow-through in-situ evaporation membranes, which have demonstrated promising potential in enhancing desalination efficiency. The use of flow-through configurations and self-heating mechanisms enables higher flux rates and reduces energy requirements, making membrane distillation an appealing option for sustainable desalination processes. These advancements shed light on the remarkable potential of membrane distillation in addressing the escalating global demand for freshwater resources.

In our previous work [19,47], we successfully fabricated a robust composite HFM from mullite-kaolinite and stainless steel (SS) as reinforcement material with promising properties. The membrane reported a much higher mechanical strength and high separation performance than its mullite counterparts and other CHFMs prepared by other low-cost materials. Therefore, this work aims to synthesize a novel omniphobic surface on the robust mullite-SS HFM surface composed of CuO nanoparticles as a surface roughness activator and the FAS organosilane as a low surface energy material by hydrothermal and fluorination techniques. Specific attention was paid in this study to the effects of varying the hydrothermal reaction times on the membrane surface

structure and appearance. The omniphobic HFMs were characterized by porosity, surface morphology, and pore size distribution. The contact angle (CA) and liquid entry pressure (LEP) measurement investigated the membrane surface wettability using three liquids with different low surface tensions; distilled water (DI) (71.9 mN/m), olive oil (31.1 mN/m) and ethanol (22.2 mN/m). The evaluation of the salt rejection rate and water flux in synthesis seawater desalination using the omniphobic HFMs was a crucial aspect of this study. Using the DCMD technique, we gained insights into the membrane's performance and potential application in tackling water scarcity. The performance of the omniphobic HFMs against fouling accumulation (post-fouling analysis) was also investigated through a feed solution containing 35 g/L NaCl feed solution and 10 g/L humic acid ($C_9H_9NO_6$) as a foulant agent with surface tension value of 58.47 mN/m. In addition, the mechanical stability of the optimum omniphobic membrane was examined for the potential leaching of elements to the permeate side. These analyses further contribute to understanding the durability and suitability of omniphobic membranes for practical applications. The selection of humic acid as an organic pollutant was justified based on its prevalence in seawater sources and resistance to conventional treatment methods. Investigating the performance of the omniphobic membranes against humic acid provides valuable insights for real-world seawater desalination applications. The physicochemical properties of humic acid, including high molecular weight and amphiphilic nature, pose challenges as a foulant, affecting membrane performance [48]. The evaluation of membrane behaviour enables the assessment of fouling resistance and anti-fouling capabilities, which are essential for MD separation processes. Moreover, humic acid's complex structure and diverse functional groups make it a representative model compound, allowing a better understanding of membrane interactions with other organic pollutants in water sources [49]. This knowledge expands the potential applicability of these membranes in water purification processes.

2. Experimental

2.1. Materials

Mullite-kaolinite was supplied from Shijiazhuang Huabang Mineral Co., Ltd. Chania and used as a ceramic material. Stainless steel alloy powder (SS, 316 L) was obtained from Sigma Aldrich Co., Ltd., USA and employed as a support material to enhance the membrane's mechanical strength. *N*-methyl-2-pyrrolidone (NMP, Sinopharm Chemical Reagent Co., Ltd., China), Arlacel (P135, Solvay Advanced Polymers, LLC), and polyethersulfone (PESf, Radel A-300, Ameco Chemicals) were used as a solvent, a dispersant and a polymer binder, respectively. Copper nitrate trihydrate ($Cu(NO_3)_2\cdot3H_2O$) was purchased from Xilong Scientific Co., Ltd., China. Ethylene glycol (EG) was purchased from Sigma Aldrich Co., Ltd., USA. Sodium hydroxide (NaOH) and ethanol were supplied from Merck, Germany, and Sinopharm Chemical Reagent Co., Ltd., China, respectively. The 1H,1H,2H,2H-perfluorodecyltriethoxysilane (C8, 97 %) was obtained from Sigma Aldrich, USA, and used as FAS grafting agent. Humic acid was purchased from Sigma Aldrich Co., Ltd., USA and used as a foulant material. Distilled and tap water was used as internal and external coagulants. Deionized (DI) water was used to prepare all required solutions.

2.2. Membrane preparation

Mullite-SS HFM was prepared by phase inversion and sintering techniques. Our earlier study detailed the membrane preparation process [19,47]. In brief, the spinning dope suspension was composed of 47 % (w/w) mullite, 10 % (w/w) SS, 35 % (w/w) NMP, 1 % (w/w) Arlacel P135 and 5 % (w/w) PESf. The extrusion and spinning conditions of the mullite-SS hollow fibre precursor were 10 mL/min extrusion rate, 10 mL/min bore fluid flow rate, and 5 cm air gap distance. The dope suspension spun through the spinneret with an internal diameter of 1 mm

and an external diameter of 2 mm and was soaked in an external coagulant (tap water) for 24 h to complete the phase inversion process [47]. Then, the mullite-SS HF precursor was dried at room temperature for 24 h. Afterwards, mullite-SS HF precursor was sintered at 1450 °C in a tubular furnace (XY-1700 MAGNA) with two steps: increasing the furnace temperature with a heating rate of 2 °C/min from room temperature to 600 °C and keeping to 2 h to remove the PESf completely, then further raising of the temperature with a heating rate of 5 °C/min to 1450 °C and maintained to 5 h to solidifying the HF precursor and forming the final mullite-SS HFM.

2.3. Hydrothermal preparation of CuO nanostructures

The preparation of CuO grafting solution on the membrane surface was achieved through the hydrothermal technique followed by the calcination process, as shown in Fig. 1. First, the preparation of the grafting solution by hydrothermal technique. 3.5 g NaOH was added to 20 mL DI water with vigorous magnetic stirring for 15 min to prepare a NaOH solution. Then, 5 g $Cu(NO_3)_2 \cdot 3H_2O$ was added to 20 mL DI water in another beaker with vigorous magnetic stirring for 10 min to prepare $(Cu(NO_3)_2 \cdot 3H_2O)$ solution. The NaOH solution and 1 g of EG were slowly added to $(Cu(NO_3)_2 \cdot 3H_2O)$ solution with vigorous magnetic stirring for 1 h to obtain a homogeneous copper oxide (CuO) gel formation with blue colour (CuO grafting solution). Afterwards, the resultant solution was transferred into a Teflon vessel in an SS autoclave. Six mullite-SS HFMs were located in the Teflon vessel at 45° with the vessel wall after sealing both ends of all HFMs. Upon hydrothermal reaction at 180 °C, a hydrothermal chemical reaction occurred between the CuO grafting solution and the membrane surface, resulting in CuO layer formation. The hydrothermal reaction was monitored for 1 to 5 h within 1 h intervals prior to the solution cooling to room temperature. The grafted mullite-SS HFMs were washed 3 times in ethanol and DI water solution with a ratio of 1:2 (w/w) to remove the unreacted free nanoparticles from the surface of mullite-SS HFMs before being dried in an oven at 60 °C for 24 h. Second, the grafted HFMs were calcined at 400 °C for 4 h in a muffle furnace. Subsequently, the grafted HFMs were washed with ethanol and DI water solution several times, dried at 60 °C overnight and kept in a dry place.

2.4. Preparation of omniphobic mullite-SS HFM

According to the literature, the two key requirements for optimum omniphobic CHFMs surfaces are low surface energy and a high membrane surface roughness structure [3,7]. These two requirements could be achieved using a surface activator material such as copper oxide (CuO) with a low surface energy of the fluoroalkylsilane (FAS) agent. The FAS agent by dip-coating technique is commonly used for CHFM omniphobocity after being modified by an activator surface agent, as previously reported in many works in literature [7,20,21]. This work used the 1H,1H,2H,2H-perfluorodecyltriethoxysilane (C8) with 97 % (w/w) concentration to modify the coated mullite-SS HFMs surfaces to omniphobic properties. The grafted mullite-SS HFMs were first immersed in ethanol and DI water solution with a ratio of 1:2 (v/v) for 24 h to increase the hydroxyl content on the membrane surface before grafting by the FAS solution. The hydroxylated process usually increases the probability of the FAS molecules reacting with the hydroxyl groups and completing the reaction on the membrane surface [50]. After overnight drying the grafted HFMs in an oven, they were immersed in the FAS solution containing 2 % (w/w) FAS and 98 % (w/w) ethanol for 48 h to ensure a complete reaction between the FAS agent and hydroxyl contents on the surfaces of membranes. Next, the HFMs were rinsed in ethanol and water several times to remove unreacted components before drying in an oven at 60 °C overnight (See Fig. 2).

The formation of the omniphobic layer on the mullite-SS HFM was composed of two key stages. The first stage was grafting the membrane surface with the CuO graft solution to increase the mullite-SS HFM roughness and solid air pockets, which increases the membrane wetting resistance. The second stage was fluorination of the mullite-SS HFM by FAS (C8) solution to reduce the membrane surface energy and the adhesion force between the membrane surface and liquid drops. Fig. 3 presents the mechanism formation of the omniphobic layer on the mullite-SS HFM.

2.5. Characterization of omniphobic mullite-SS HFM

The membrane morphology was observed by scanning electron microscopy (SEM) (model Hitachi, TM3000). The membrane surface roughness (Ra) was investigated by atomic force microscopy (AFM) (PARK XE-100). The porosity, pore size, and pore size distribution were determined by mercury intrusion porosimetry (MIP) (AutoPore9510, USA). The element compositions on the membrane surface were conducted using dispersive energy X-ray (EDX) (HITACHI 8230). The membrane wetting property was obtained by contact angle measurement using the sessile drop method (OCA 15EC, Dataphysics, Germany) for five duplication times. The permeation setup evaluated the membrane's water liquid entry pressure (LEP) five duplication times. A
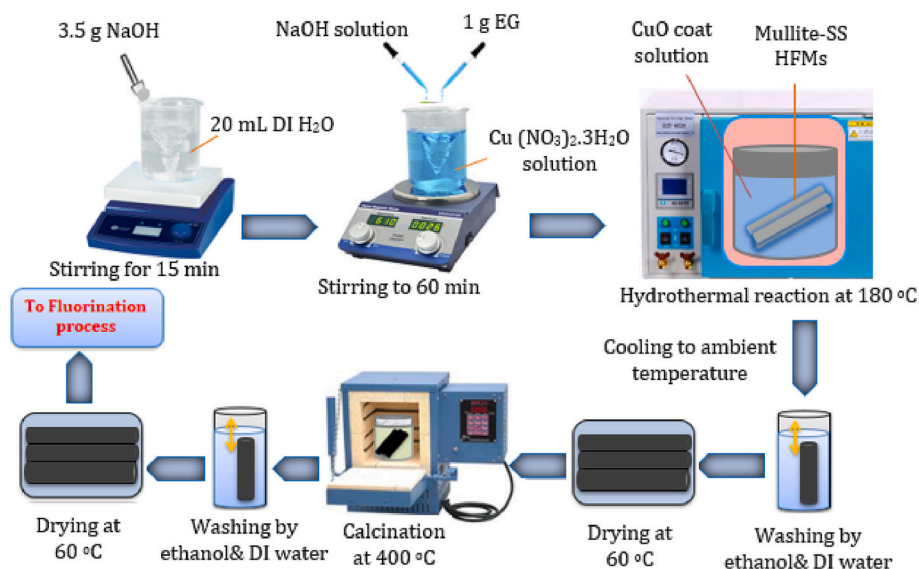

Fig. 1. Schematic diagram of hydrothermal synthesis of CuO nanostructure graft solution on mullite-SS HFM surface.
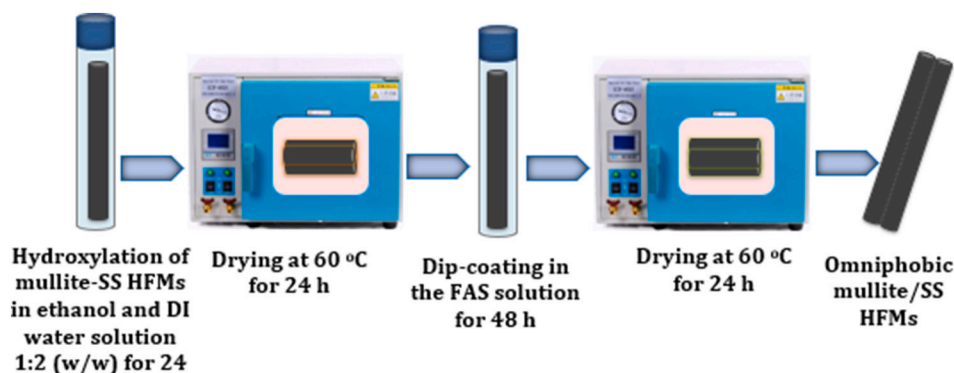
Fig. 2. Schematic diagram of omniphobic mullite-SS HFMs preparation.

contact angle goniometer (OCA 15 EC, Dataphysics) evaluated the contact angle measurement on the membrane surface.

2.6. DCMD test

In this study, the lab scale DCMD set-up was used to test the performance of the omniphobic mullite-SS HFMs for water desalination (see Fig. 4). The performance test and omniphobic layer stability were examined for three omniphobic mullite-SS HFMs for 10 h using a feed solution containing a syntheses seawater with a 35 g/L salt concentration and 10 mg/L humic acid were added to the feed solution to evaluate the resistance of the membranes to the organic fouling. The DCMD system was composed of a hot stream which contained the feed solution that flowed in the lumen of the membranes at 80 °C and 0.3 L/min, whereas the cold stream contained deionized water flowed on the shell of the membranes at 10 °C and 0.1 L/min. A coiled heater controlled the hot stream, while the cold stream was controlled by a chiller. A weighing balance obtained the weight difference of the cold water tank, and the permeate flux was estimated by Eq. (1) [51–53].

$$J_v = \frac{\Delta W}{A \Delta t} \qquad (1)$$

Where J_v (kg/m^2·h): permeate flux, ΔW (kg): weight difference at time t (h), and A: membranes effective area (m^2).

The performance of salt rejection was estimated by Eq. (2):

$$R(\%) = \left(1 - \frac{C_P}{C_F}\right) \times 100\% \qquad (2)$$

Where R (%): Salt rejection rate, C_F (mol/L): Feed solution concentration, and C_P (mol/L): Permeate concentration. C_f and C_p were measured by a conductivity meter based on the dilution effect [53]:

$$C_{P=} \frac{C_1 m_1 - C_0 m_0}{m_1 - m_0} \qquad (3)$$

Where m_o: initial permeate mass; m_1: final permeate mass; C_o initial permeate salt concentration; C_1: final permeate salt concentrations. C_o and C_1 were found using a conductivity meter based on the dilution effect [53]:

3. Results and discussion

Omniphobic mullite-SS HFMs with different hydrothermal reaction times ranging from 1 to 5 h were successfully synthesized using the CuO graft solution. The effect of omniphobic and hydrophobic layers formation on the physical and wetting properties of mullite-SS HFMs and testing these HFMs in the DCMD system were discussed as follows:

3.1. The physical and wetting properties of mullite-SS HFMs

In this study, the morphology and structure of hydrophobic mullite-SS HFM (M-SS,0 h/FAS) and all omniphobic mullite-SS HFMs (M-SS,1–5 h/FAS) prepared at different reaction times were evaluated through SEM analysis, as presented in Fig. 5(A–F). All omniphobic HFMs were studied based on the impacts of hydrothermal reaction times on the distribution rate of the CuO molecules on the membrane surface. The SEM images of the microstructural differences studied by the CuO reaction time change on the membrane surface through a 1 h interval are exhibited in Fig. 5(B–F). The M-SS,1 h/FAS, M-SS, 2 h/FAS, M-SS, 3 h/FAS, M-SS, 4 h/FAS and M-SS, 5 h/FAS refers to omniphobic mullite-SS HFMs prepared at 1, 2, 3, 4 and 5 h hydrothermal reaction time. Overall, Fig. 5(B–F) demonstrates that the CuO particle size on the outer surface of the mullite-SS HFM increment with increasing the hydrothermal reaction time (i.e. 1, 2, 3, 4, and 5 h). There was no discrete appearance on the membrane surface at a hydrothermal reaction time of less than 1 h. Some combined CuO nanoparticles with no shape were only seen on the outer surface. This observation could be attributed to the insufficient hydrothermal reaction time between the CuO nanoparticles and the outer membrane surface. After the reaction time reached 1 h, an obvious few aggregated small leaf-like CuO particles on the outer surface were observed, and the CuO nanoparticles did not entirely cover the outer membrane surface (Fig. 5B). The growth of the CuO nanoparticles on the outer surface increased clearly with the increase in hydrothermal reaction times. The longer reaction times lead to the formation of larger nanoparticles on the membrane surface. This is because the longer reaction time allows more time for the CuO nanoparticles to grow and for the particles to coalesce, leading to larger particles. Longer reaction times also lead to a more uniform distribution and uniform, well-defined shapes.

In addition, the increase in the leaf-like CuO particles on the outer surface was observed within the reaction times of 2, 3, and 4 h, as shown in Fig. 5(C, D, and E). The hydrothermal reaction time of 4 h (Fig. 5, E) was sufficient for an obvious leaf-like formation, where the observed leaves on the outer surface were like leaves, as seen in Fig. 5(E). The leaf-like structures of several sizes grew almost regularly on the mullite-SS HFM (see Fig. 5D and E). However, the change in the structure of the membrane's outer surface was observed by increasing the hydrothermal reaction time over 4 h (i.e., 5, 6, etc.). For example, increasing the hydrothermal reaction time to 5 h led to the loss of the leaf-like structure and some deformations on the outer surface of the membrane, such as large cracks that could affect its rejection performance, as shown in the microscopy image in Fig. 5(F). This observation could be due to the long hydrothermal reaction that affected the membrane surface formation and changed the outer surface morphology. Longer hydrothermal reaction times facilitate the increased growth and aggregation of CuO nanoparticles on the membrane surface, leading to a rougher and more irregular surface structure. This phenomenon impacts the interfacial
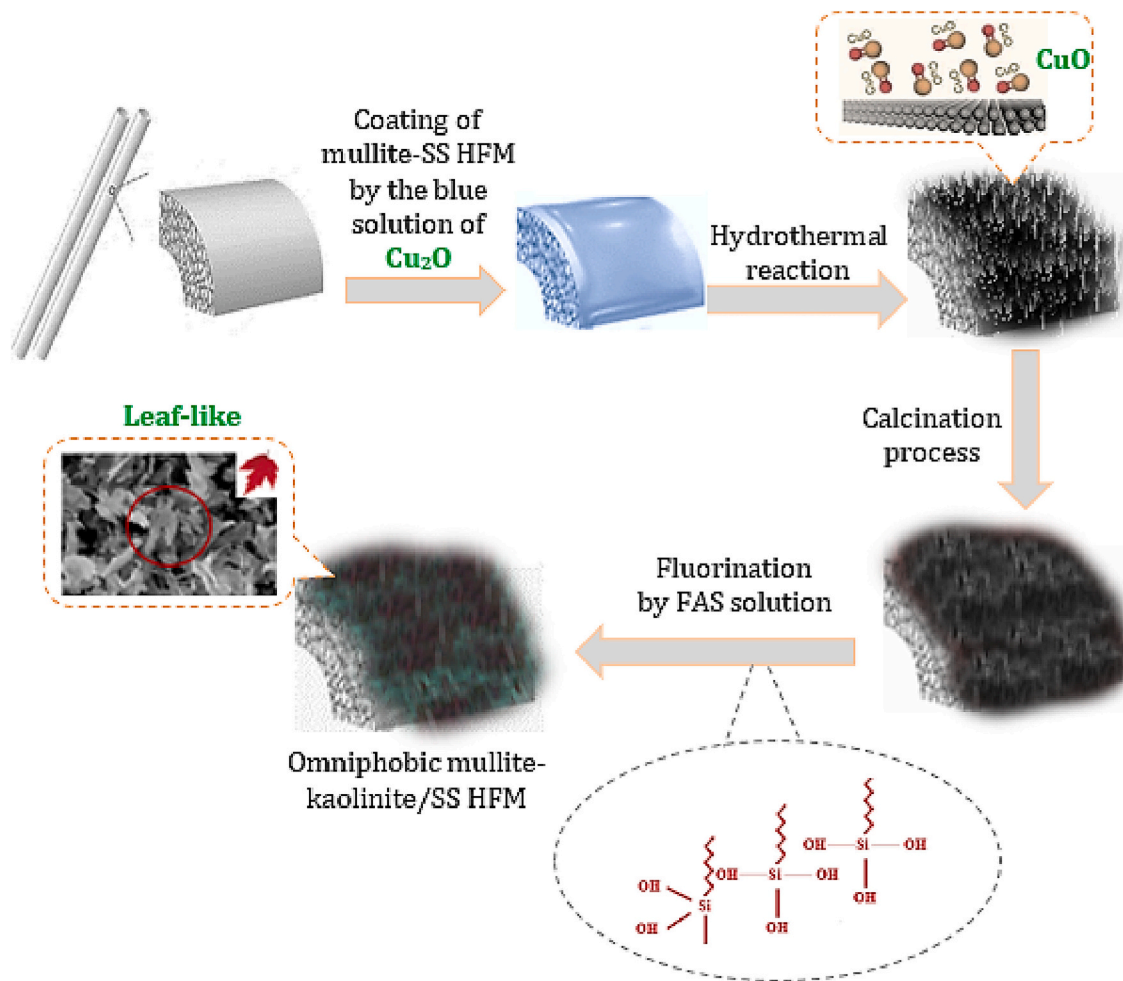
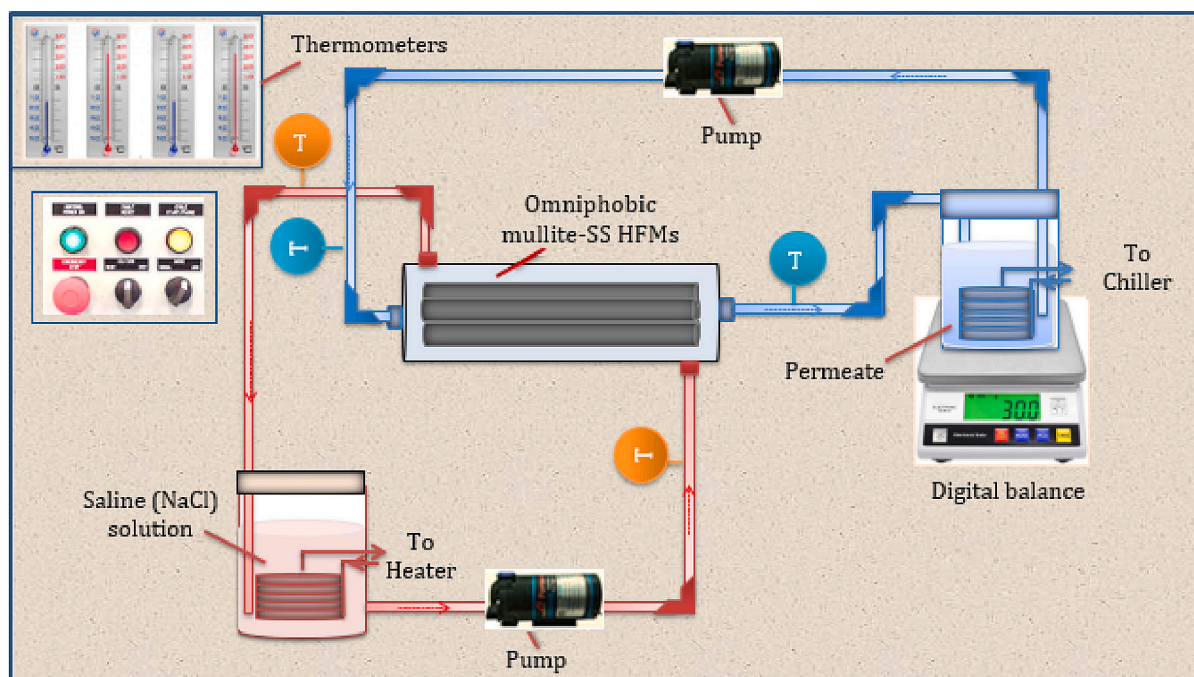**Fig. 3.** Schematic diagram of omniphobic layer formation on the mullite-SS HFM surface.

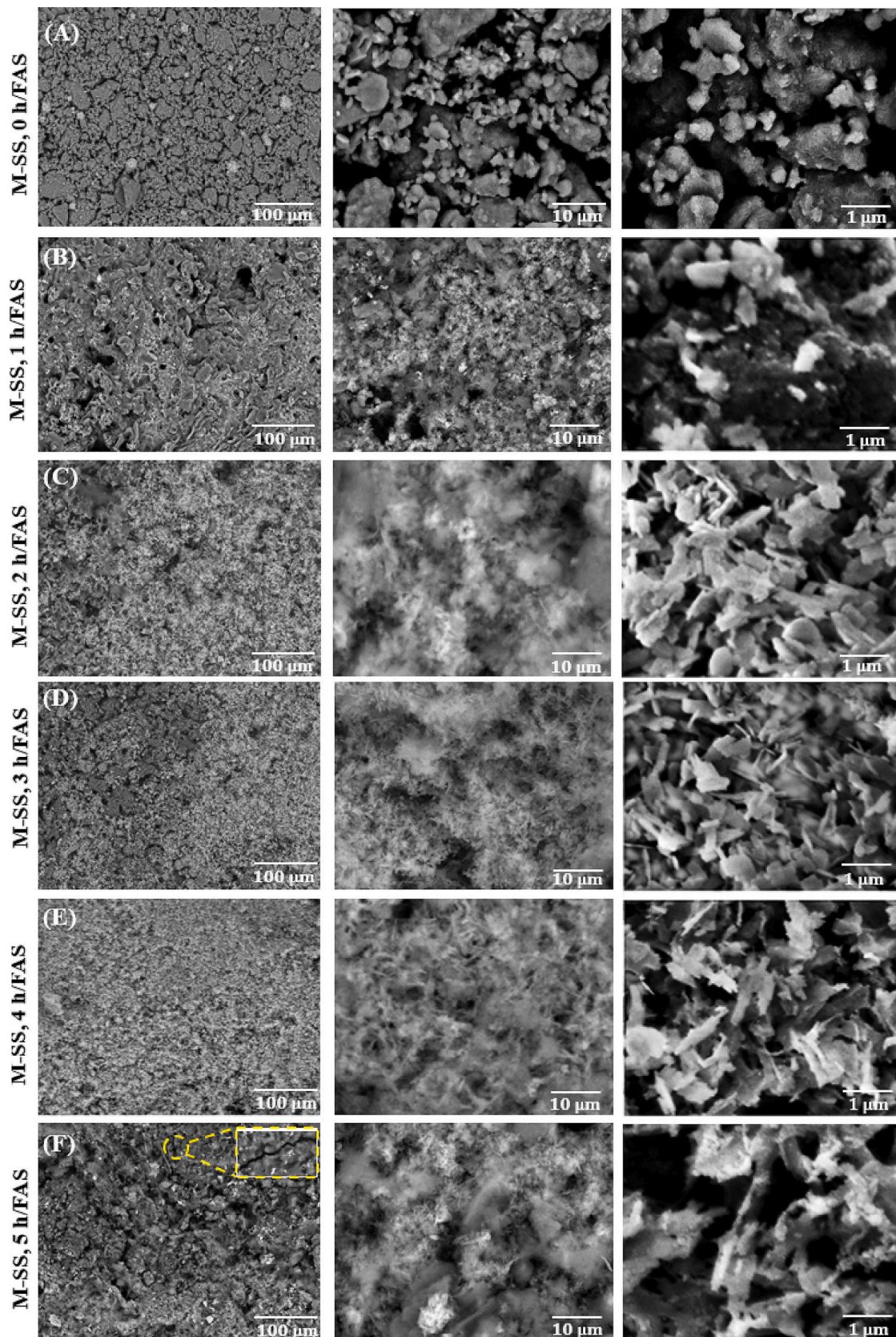**Fig. 4.** Schematic diagram of lab scale DCMD desalination system.

Fig. 5. SEM images of (A) hydrophobic M-SS,0 h/FAS and all omniphobic mullite-SS HFMs prepared at different hydrothermal reaction times: (B) M-SS,1 h/FAS, (C) M-SS, 2 h/FAS, (D) M-SS, 3 h/FAS, (E) M-SS, 4 h/FAS and (F) M-SS, 5 h/FAS at 180 °C hydrothermal reaction temperature [M: Mullite].
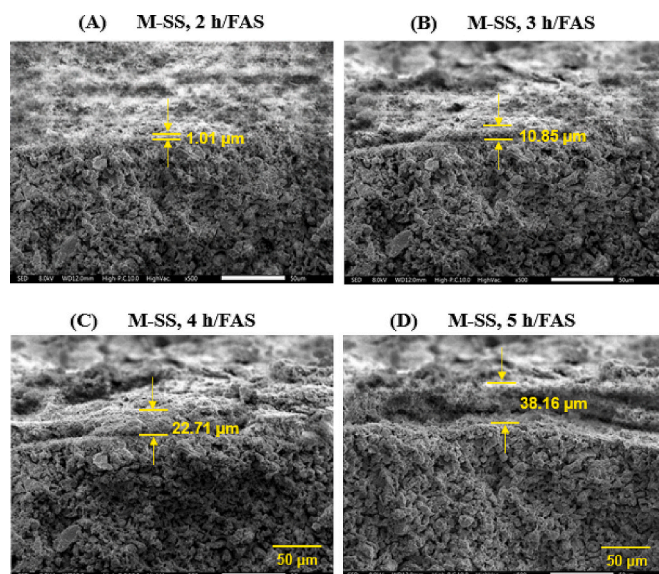
Fig. 6. SEM images of the cross-section of (A) M-SS,2 h/FAS, (B) M-SS, 3 h/FAS, (C) M-SS, 4 h/FAS and (D) M-SS, 5 h/FAS.

interaction between the CuO layer and the membrane surface, influencing the stability and durability of the omniphobic layer. Consequently, several defects, such as cracking, may arise on the membrane's surface (See Fig. 5F). Therefore, maintaining a delicate balance between achieving the desired surface roughness and ensuring a stable interface is crucial for reliable performance over prolonged operation periods.

The mullite-kaolinite HFM of M-SS,4 h/FAS, and M-SS,3 h/FAS had more intense and better covered CuO layer than the M-SS,1 h/FAS, M-SS,2 h/FAS, and M-SS, 5 h/FAS membranes, as presented in the SEM results in Fig. 5(B–F). It can be concluded that the best microscopy image was observed on the outer membrane surface of mullite-kaolinite at 4 h/FAS with a leaf-like structure and better-covered CuO layer on the outer surface compared to other omniphobic membranes prepared at other reaction times of 1, 2, 3 and 5 h.

The effects of different hydrothermal reaction times (i.e., 2, 3, 4, and 5 h) on the cross sections of the omniphobic mullite-SS composite have also been investigated. The results of this investigation are presented in Fig. 6, where SEM images of the cross-sections are displayed. Interestingly, at a hydrothermal reaction time of 1 h, the layer thickness was too thin to be accurately measured. However, the thinnest measured layer thickness of 1.01 μm was obtained at the shortest reaction time of 2 h. As the hydrothermal reaction time increased, the thickness of the omniphobic layer also increased. This relationship is evident from the layer thickness measurements obtained at reaction times of 3, 4, and 5 h, which were 10.85 μm, 22.71 μm, and 38.16 μm, respectively. The gradual increase in layer thickness strongly suggests a direct correlation between the reaction time and the resulting thickness of the omniphobic layer. This observed phenomenon can be attributed to the influence of hydrothermal reaction times on the growth of CuO nanoparticles on the

outer membrane surface. These nanoparticles, as depicted in Fig. 5 (C–F), play a critical role in enhancing the thickness of the omniphobic layer.

EDX analysis was used to characterize the elemental composition of the surfaces of the hydrophobic and omniphobic surface-modified mullite-SS HFMs prepared at different hydrothermal reaction times before the MD test, as shown in Table 1. The elemental mapping was also used to investigate the CuO nanoparticles distribution on the membrane surface of omniphobic HFMs from 1 to 5 h, as exhibited in Fig. 7(A–F). From Table 1, M-SS,0 h/FAS, the highest elements content in the hydrophobic M-SS,0 h/FAS was the mullite contents of oxygen at 29 % (w/w), aluminium at 22.5 % (w/w), and silicon at 20 % (w/w), while the other elements with smaller contents of fluorine (F, 3.8 % (w/w)) and SS alloy elements. However, Table 1 (M-SS,1–5 h/FAS) and Fig. 7(B–E) showed the most abundant compounds in all omniphobic HFMs were the composition of CuO, which was copper (Cu, dark purple) and oxygen (O, dark red), consisting of the surface chemistry of all omniphobic HFMs. This result indicated the effective CuO nanoparticles deposition on the surfaces of the omniphobic HFMs through the hydrothermal step. The atomic ratios of O/Cu in all omniphobic HFMs at different reaction times of 1, 2, 3, 4, and 5 h were 2.31, 1.99, 1.56, 1.33 and 1.16, respectively (Table 1 (M-SS,1–5 h/FAS)). The highest atomic number of Cu (25.2 % (w/w)) was observed at omniphobic M-SS HFM at 4 h/FAS, with an O atomic number of 33.4 % (w/w), as confirmed by CuO nanoparticles distribution in Table 1 (M-SS,4 h/FAS) and Fig. 7 D. Other elements composed of mullite-SS HFMs, such as Si, Al, Fe, Cr, Ni and Mn, were also observed with almost identical on the surfaces of omniphobic HFMs with different contents and distribution (see Table 1 & Fig. 7).

The fluorine elements (F, light purple) on the surfaces of all omniphobic HFMs were also observed, with different atomic contents ranging from 7.4 to 9.0 % (w/w) (see Table 1 (M-SS,1–5 h/FAS)). The presence of the fluorine elements indicated the existence of hydrophobic functional groups on the surfaces of all omniphobic HFMs. The highest fluorine contents of 9.0 % (w/w) (Table 1) (M-SS,4 h/FAS) were observed at omniphobic M-SS HFM at 4 h/FAS, whereas the lowest fluorine contents of 7.4 % (w/w) were obtained at omniphobic M-SS HFM at 5 h/FAS (Table 1) (M-SS,5 h/FAS). This observation could be ascribed to the lowest FAS contents on the membrane surface or the insufficient chemical reaction between FAS and the membrane surface. The carbon elements (C, dark brown) were also found on the surfaces of all omniphobic HFMs. The formation of C could be attributed to the hydrothermal reaction between the membrane surface and the CuO graft solution.

The crystallinity of all modified mullite-SS HFMs was characterized by XRD analysis, as presented in Fig. 8. Noticeably, there was a reduction in the crystallinity of mullite, cristobalite and nichrome of all omniphobic mullite-SS HFMs compared to the hydrophobic M-SS,0 h/FAS, indicating the successful deposition of CuO nanoparticles on the surfaces of HFMs. Several CuO peaks were exhibited in the XRD pattern at different 2θ values. The number of CuO peaks differed due to the slight effect of the hydrothermal reaction times. At M-SS, 4 h/FAS and M-SS, 5 h/FAS, the CuO peaks were observed at 2θ values of 9.2°, 18.2°, 32.0°, 36.3°, 40.7° and 41.1°, while at 1 h/FAS, M-SS, 2 h/FAS, M-SS, 3

Table 1
Elemental composition on the surface of all modified mullite-SS HFMs.

Membrane code	Elements content (wt%) in the membrane surface							
	Si	Al	Cu	F	O	Fe	Cr	Ni
M-SS,0 h/FAS	20.0	22.5	–	7.4	29.9	3.8	4.9	0.8
M-SS,1 h/FAS	9.3	9.2	13.6	9.0	31.5	6.4	1.7	0.8
M-SS, 2 h/FAS	4.6	4.7	14.7	7.9	29.3	3.8	0.9	0.5
M-SS, 3 h/FAS	7.5	8.2	22.5	8.2	35.1	6.1	1.7	0.8
M-SS, 4 h/FAS	7.1	5.9	25.2	8.1	33.4	5.2	1.4	0.6
M-SS, 5 h/FAS	9.1	6.7	24.9	7.4	28.9	5.2	1.4	0.6

Note: Si: silicon; Al: aluminium; Cu: copper; F: fluorine; O: oxygen; Fe: iron; Cr: chromium; Ni: nickel.
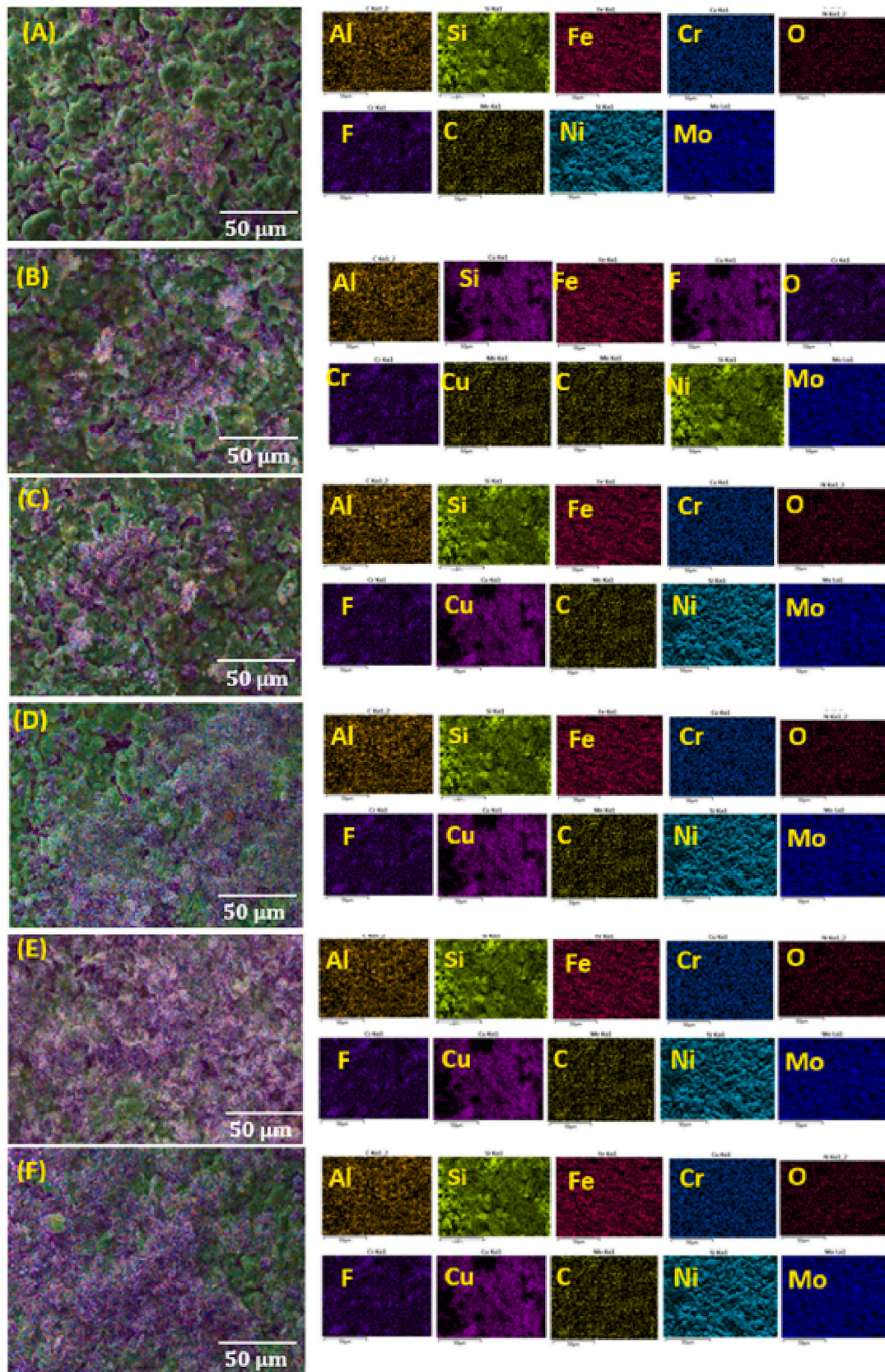
Fig. 7. EDX analysis on the surface of (A) hydrophobic M-SS,0 h/FAS HFM and all omniphobic mullite-SS HFMs; (B) M-SS,1 h/FAS, (C) M-SS, 2 h/FAS, (D) M-SS, 3 h/FAS, (E) M-SS, 4 h/FAS and (F) M-SS, 5 h/FAS.
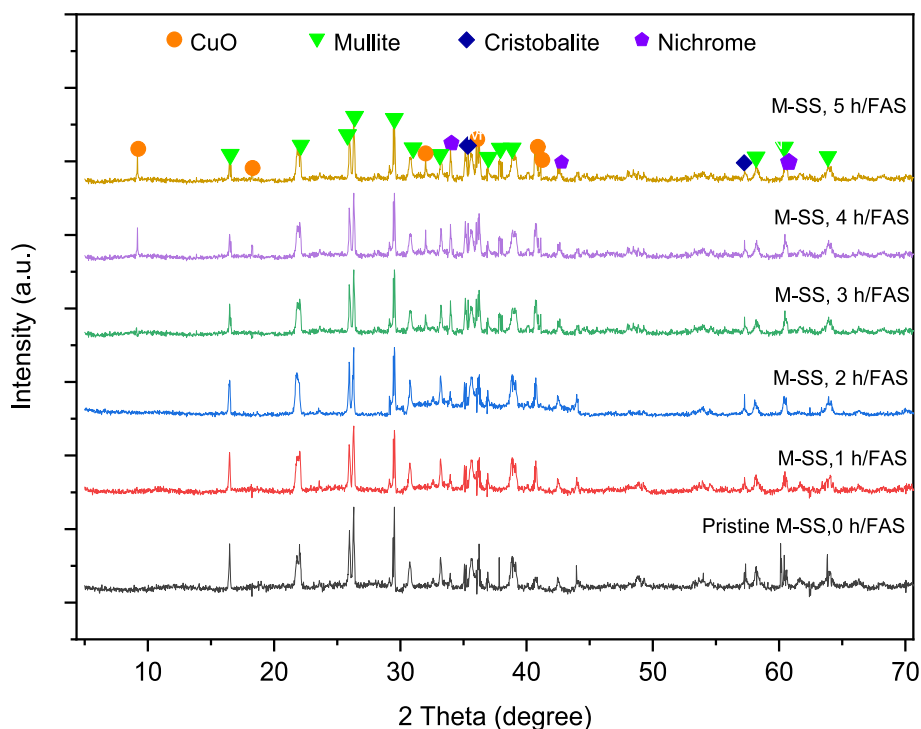
Fig. 8. XRD analysis of the surfaces of hydrophobic M-SS,0 h/FAS HFM and all omniphobic mullite-SS HFMs by CuO nanostructure at different hydrothermal reaction times M-SS,1 h/FAS, M-SS, 2 h/FAS, M-SS, 3 h/FAS, M-SS, 4 h/FAS and M-SS, 5 h/FAS.
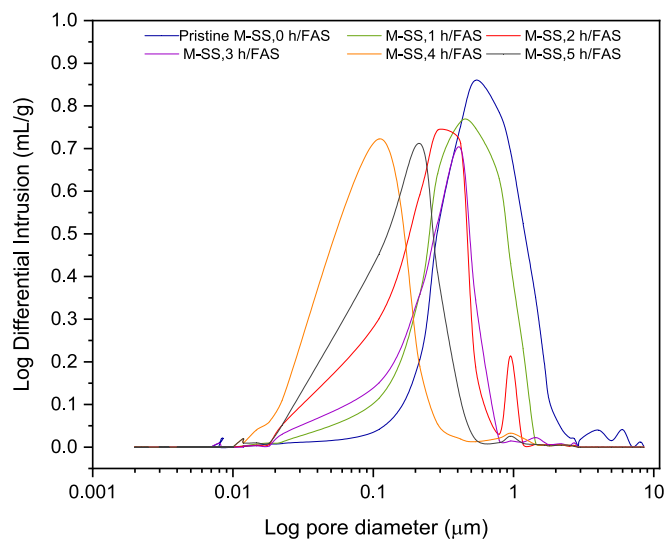

Fig. 9. Pore size distribution of hydrophobic M-SS,0 h/FAS HFM and all omniphobic mullite-SS HFMs; M-SS,1 h/FAS, M-SS, 2 h/FAS, M-SS, 3 h/FAS, M-SS, 4 h/FAS and M-SS, 5 h/FAS.

Fig. 10. Porosity and mean pore sizes of hydrophobic M-SS,0 h/FAS HFM and omniphobic mullite-SS HFMs; M-SS,1 h/FAS, M-SS, 2 h/FAS, M-SS, 3 h/FAS, M-SS, 4 h/FAS and M-SS, 5 h/FAS [].

h/FAS were observed at 32.0°, 36.3°, 40.7° and 41.1°. These results could be attributed to the higher CuO nanoparticles contents (wt%) on the surfaces of the M-SS, 4 h/FAS and M-SS, 5 h/FAS. This observation was consistent with the EDX results in Fig. 7D & E. In addition, the CuO peaks at 2θ values of 32.0°, 36.3°, 40.7° and 41.1° were similar to that mentioned elsewhere in the literature [54]. No peaks of other compounds were observed on the surfaces of all omniphobic HFMs, as evidenced in the XRD pattern, demonstrating the success of the hydrothermal technique in producing CuO with high purity.

The effect of the hydrophobic and omniphobic layers prepared by the CuO and hydrothermal process on the pore size distribution on surfaces
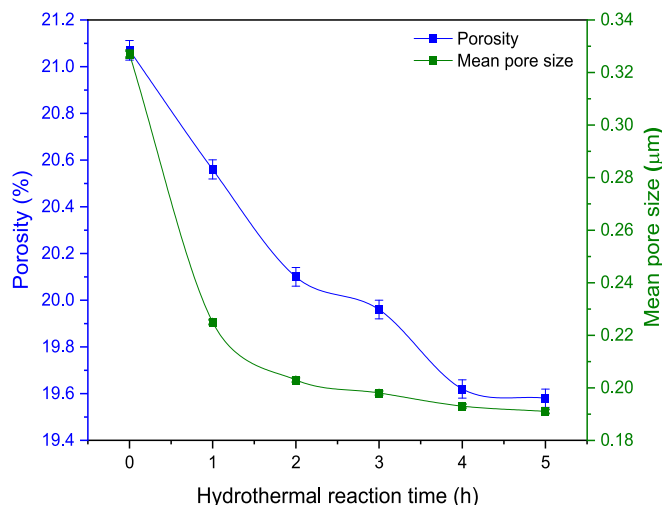
of mullite-kaolinite HFMs was studied through MIP analysis based on the log scale, as shown in Fig. 9. It can be seen that at the hydrophobic mullite-kaolinite HFM, the highest number of pores was observed, while omniphobic mullite-SS HFMs showed a lower number of pores with different levels due to the formation of omniphobic layers on the surfaces of HFMs. All omniphobic mullite-SS HFMs also exhibited a different number of pores. This outcome could be ascribed to the effect of the hydrothermal reaction times, which increased the growth of CuO nanoparticles on the membrane surface, as proved in Fig. 6(B–F). The highest peak among all omniphobic mullite-SS HFMs was obtained at M-SS,1 h/FAS, with a higher number of pores, whereas the lowest peak was obtained at M-SS,5 h/FAS, with a lower number of pores. At M-SS,4 h/FAS and M-SS,5 h/FAS had almost the same peak height with a slight

difference in the number of pores. This observation could be due to no obvious effect of the hydrothermal reaction time after 4 h. Since some investigations in the literature reported that the pore sizes for hydrophobic membranes used for MD applications typically range from 0.1 to 1.0 μm, and the pore size should be less than 0.5 μm to avoid membrane pore wetting [55,56]. Thus, the best pore sizes range was obtained from 0.012 to 0.45 μm for M-SS,4 h/FAS, which appears the most appropriate for the MD applications.

The porosity and mean pore size of the hydrophobic and all omniphobic mullite-SS HFMs were also evaluated by MIP analysis, as presented in Fig. 10. From Fig. 10, the hydrophobic M-SS,0 h/FAS showed the highest porosity and largest mean pore size at 21.07 % and 0.327 μm, respectively. On the other hand, a slight difference in the porosity and mean pore size was observed among all omniphobic mullite-SS HFMs. Increasing the hydrothermal reaction time led to a slight decrease in porosity and mean pore size due to increasing the growth of the CuO nanoparticles on the membrane surface. This effect of the hydrothermal reaction time was observed elsewhere in the literature [21]. The highest and lowest porosity and mean pore size was obtained at M-SS,1 h/FAS and 5 h/FAS, respectively. In general, the hydrothermal process significantly impacted the porosity and the pore size of all omniphobic HFMs. Despite this, the omniphobic HFMs still displayed porosity from 19.58 to 20.56 % and pore size from 0.191 to 0.225 μm satisfactory for MD applications.

Fig. 11(A–F) demonstrates the three-dimensional AFM micrographs of the outer surfaces of hydrophobic and all omniphobic mullite-SS HFMs. This analysis is significant for determining the membrane surface roughness to ensure high membrane omniphobicity and anti-wetting performance in the presence of a low surface energy material

such as FAS. Increasing the surface roughness usually decreases the contact area between liquid drops and the membrane surface due to the presence of the air pocket at the membrane/liquid interface, which works as an omniphobic layer, as Ni et al. [57] reported. As seen in Fig. 11(A–F), there is an obvious increment in the surface roughness after the surface modification to omniphobic properties (Fig. 11(B–F)). The membrane roughness increased clearly from the hydrophobic M-SS,0 h/FAS of 0.286 μm to 0.341 μm after 1 h reaction time, which is consistent with a previous observation by Twibi et al. [21]. In addition, AFM analysis determined the multilevel roughness with the different hydrothermal reaction times, as presented in Fig. 11(B–F). A gradual increase in the surface roughness values from 0.341, 0.464, 0.521, 0.798 to 0.690 μm was observed with increasing the hydrothermal reaction times from 1, 2, 3, 4 to 5 h, reflecting the attachment of micro-levels CuO particles on the membrane surface and which acted as a secondary structure increased the surface roughness with increasing the hydrothermal reaction times. The highest surface roughness of 0.798 μm was obtained at M-SS, 4 h/FAS, which could be attributed to the more rapid growth of CuO nanoparticles, producing greater coverage on the membrane surface, resulting in higher roughness, as shown in Fig. 5E. Another significant observation was that the value of M-SS, 5 h/FAS surface roughness of 0.690 μm was reduced to less than at M-SS, 4 h/FAS, which could be due to improper CuO nanoparticles growth in some spots on the membrane surface due to some large cracks on the omniphobic layer which affected the surface roughness, as demonstrated in Fig. 5F. When the omniphobic layer contains cracks, the overall roughness of the surface can be reduced because the cracks can create clear areas depending on the width of the cracks on the omniphobic layer, reducing the membrane roughness.
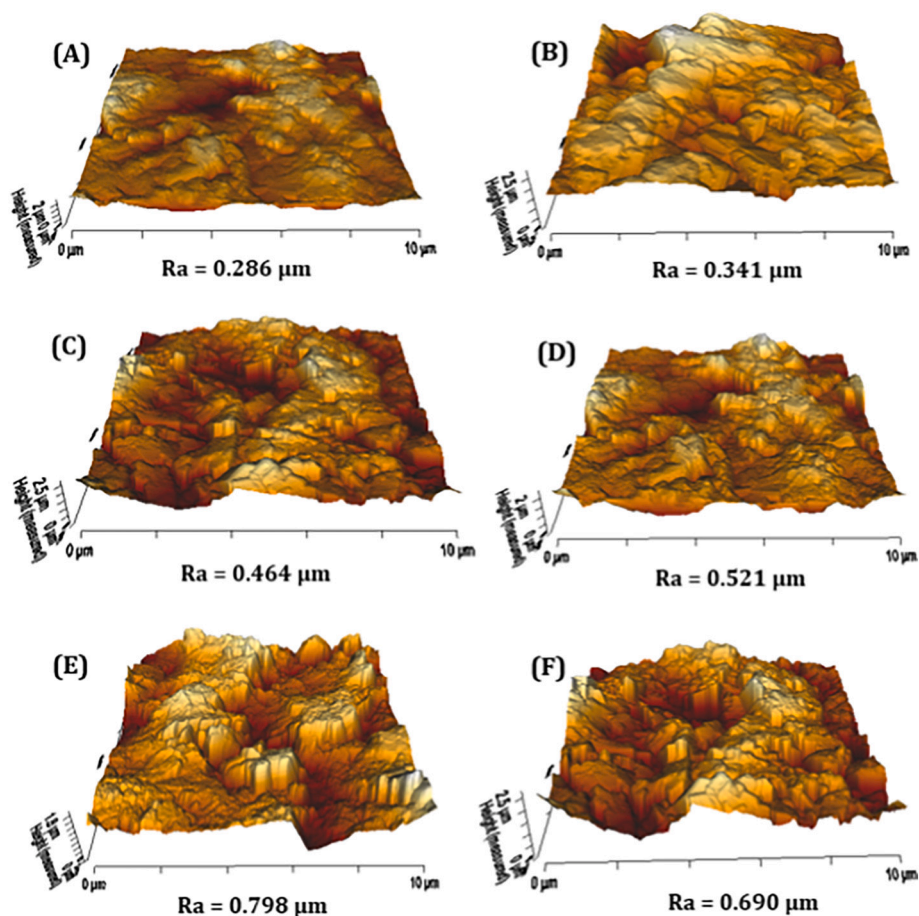

Fig. 11. Three-dimensional AFM micrographs of the outer surfaces of (A) hydrophobic M-SS,0 h/FAS HFM and all omniphobic mullite-SS HFMs; (B) M-SS,1 h/FAS, (C) M-SS, 2 h/FAS, (D) M-SS, 3 h/FAS, (E) M-SS, 4 h/FAS and (F) M-SS, 5 h/FAS.

Contact angle (CA) is a significant wetting property that should be measured on any membrane surface before being used for MD processes to determine its ability against wetting potential by different liquid drops. Therefore, the surface wettability of the pristine, hydrophobic and omniphobic HFMs was investigated through the CA measurement test using sessile liquid drops of 1 μL. Three liquids with different surface tensions of distilled water (DI) (71.9 mN/m), olive oil (31.1 mN/m) and ethanol (22.2 mN/m) were selected for this test, and the outcomes were exhibited in Fig. 12. The values of the CAs of the pristine mullite-SS HFM were not shown in Fig. 12 because it was zero due to the rapid spread of liquid into the HFMs, causing a difficult CA measurement. As seen in Fig. 12, the lowest CA values for water (138°), ethanol (56°) and olive oil (34°) were determined at hydrophobic M-SS,0 h/FAS HFM. As for the CAs of omniphobic HFMs, a gradual increase in the CAs values of all liquids was obtained with increment in the hydrothermal reaction time from 1 to 4 h, while at 5 h, a reduction in the CAs was observed compared to CAs at 4 h.

Since the membrane surface is considered superomniphobic when the water CA exceeds 150°, it is also considered omniphobic when the CAs of water and oil are 140° and 110°, respectively, as Zheng et al. [58] reported. In addition, it is considered super-omniphobic when the membrane surface CA exceeds 150° with almost all low and high-surface tension liquids such as alcohols, oils, and organic solvents [14]. Therefore, the M-SS,0 h/FAS and M-SS,1 h/FAS HFMs showed hydrophobic properties, M-SS, 2 h/FAS and M-SS, 3 h/FAS HFMs exhibited omniphobic properties for all liquids (i.e., DI water, olive oil and ethanol). However, both the M-SS, 4 h/FAS and M-SS, 5 h/FAS, demonstrated super-omniphobic properties for DI water. In addition, M-SS, 4 h/FAS,

showed super-omniphobic properties for olive oil and omniphobic properties for ethanol, while M-SS, 5 h/FAS omniphobic properties for only olive oil. The M-SS 4 h/FAS with the leaf-like structure displayed the highest super-omniphobic properties with 167° DI water CA, 152° olive oil CA and 145° ethanol CA. This result could be attributed to producing the hierarchical structure on the membrane surface, which increased the membrane roughness, closely packed CuO nanoparticles (see Fig. 5E) and trapping air between CuO nanoparticles, keeping the Cassie-Baxter state and forming an outstanding re-entrant structure and the fluorination of the membrane surface by FAS. Furthermore, it could be due to the change in the surface of pore size resulting from increasing the growth of CuO nanoparticles on the membrane surface with increasing the hydrothermal reaction time. For the same reasons, the highest LEP value of 5.4 and 5.2 bar was observed at M-SS, 4 h/FAS and M-SS, 5 h/FAS, respectively, as seen in Table 2.

Fig. 13. shows the effect of the omniphobic layer and hydrothermal reaction times (i.e. 1, 2, 3, 4 and 5 h) on the mechanical strength of all omniphobic mullite-SS HFMs. As seen in Fig. 13, there was an obvious increase in the mechanical strength with increasing the reaction time from 0 to 5 h. The mechanical strength of the hydrophobic M-SS,0 h/FAS HFM of 107 MPa, increased to 108.7 MPa after 1 h hydrothermal reaction time. After 2 h, the mechanical strength increased to about 110.3 MPa, while after 3 h, a slight increase to 110.9 MPa was observed compared to after 2 h reaction time. As for the values of the mechanical strength after 4 and 5 h increased to about 114 and 113.6 MPa, respectively. The observed gradual increase in mechanical strength could be due to the increased packing and stacking of CuO nanoparticles with increasing reaction time. In addition, it could be ascribed to the
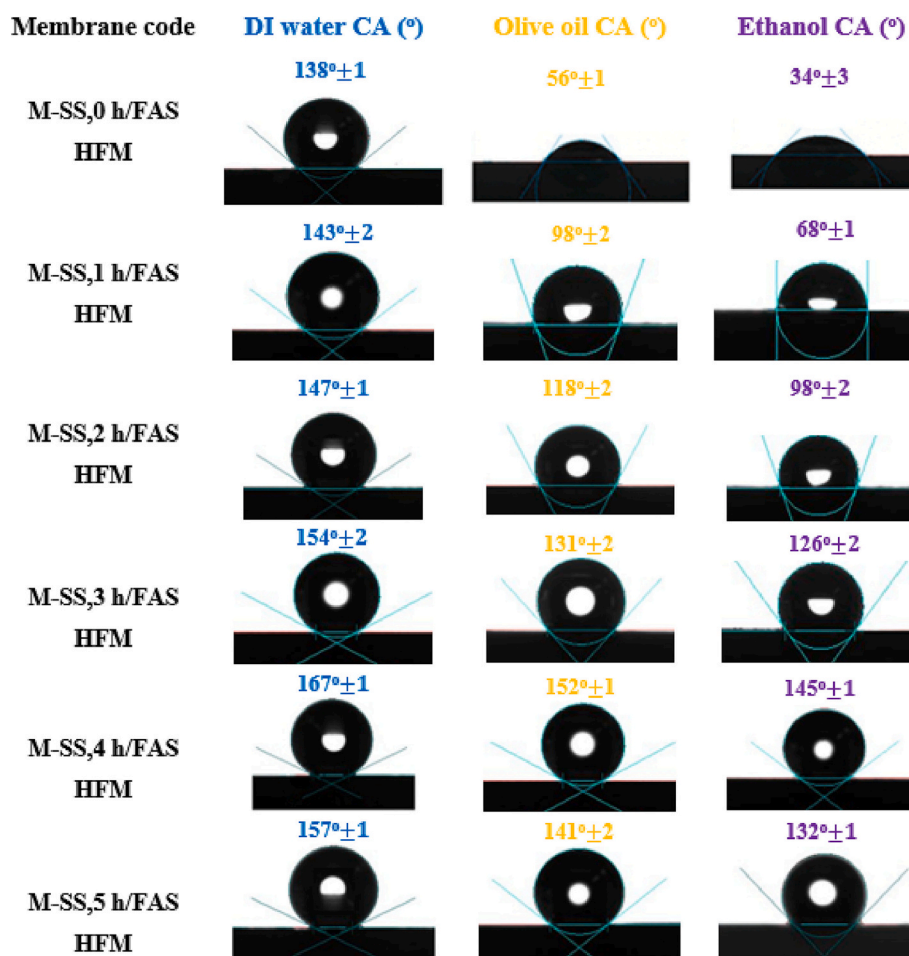

Fig. 12. Contact angle measurements for hydrophobic M-SS,0 h/FAS HFM and omniphobic mullite-SS HFMs; M-SS,1 h/FAS, M-SS, 2 h/FAS, M-SS, 3 h/FAS, M-SS, 4 h/FAS and M-SS, 5 h/FAS [notice: error bars are based on standard errors from four duplicate calculations].

Table 2
LEP values of hydrophobic M-SS,0 h/FAS, M-SS,1 h/FAS, M-SS,2 h/FAS, M-SS,3 h/FAS, M-SS,4 h/FAS and M-SS,5 h/FAS [error bars are based on standard errors from three duplicate calculations].

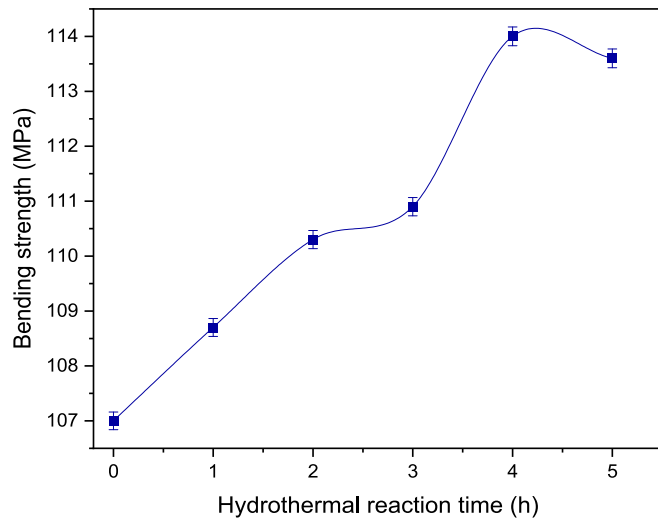| Membrane code	M-SS 0 h/FAS	M-SS 1 h/FAS	M-SS 2 h/FAS	M-SS 3 h/FAS	M-SS 4 h/FAS	M-SS 5 h/FAS
LEP (bar)	2.1 ± 1.2	2.7 ± 1.1	3.6 ± 2.1	4.9 ± 2.0	5.4 ± 1.1	5.2 ± 1.4

Fig. 13. Bending strength of hydrophobic M-SS,0 h/FAS,0 h, M-SS,1 h/FAS, M-SS, 2 h/FAS, M-SS, 3 h/FAS, M-SS, 4 h/FAS and M-SS, 5 h/FAS [notice: error bars are based on standard errors from four duplicate calculations].

effect of different hydrothermal reaction times on the loading of CuO on the surfaces of HFMs (see Fig. 7, E & F), which increased with time, as seen in Table 3. Table 3 presents mass membrane measurements before and after the hydrothermal process.

The mechanical stability and potential leaching of nanoscale Cu elements from all omniphobic layers prepared with varying hydrothermal reaction times were also investigated. The samples were subjected to a 30-min ultrasonication treatment in Milli-Q water to examine leaching. Subsequently, the water samples were analyzed using an Agilent 710 Series ICP-OES, an inductively coupled plasma optical emission spectroscopy analyzer, to detect any leaching of CuO [59]. The analysis of CuO was conducted at a wavelength of 324.750 nm. The outcomes of the

mechanical stability test are presented in Table 3. Findings revealed significant leaching of Cu elements in M-SS, 2 h/FAS, M-SS, 2 h/FAS, and M-SS, 3 h/FAS, indicating the low mechanical stability of these omniphobic membranes. However, about no leaching of Cu elements in the omniphobic layer prepared with a 4 h hydrothermal reaction time, demonstrating high structural stability in M-SS, 4 h/FAS, and a strong attachment of CuO particles to the membrane surface. Furthermore, the omniphobic layer in M-SS, 5 h/FAS, exhibited higher mechanical stability than those prepared with 1, 2, and 3 hydrothermal reaction times, as seen in Table 4.

3.2. The performance of the modified membranes in DCMD

The performance of the hydrophobic and omniphobic mullite-SS HFMs prepared at different hydrothermal reaction times was tested for long-time operation of 24 h using a feed solution containing a synthetic seawater 35 g/L NaCl and 10 mg/L humic acid as a foulant agent at 80 °C via DCMD system, and the results were exhibited in Fig. 14(A–F). In this test, the vapour flux and salt rejection rate were monitored within 0.5 h intervals. As seen in Fig. 14(A–F), the initial vapour flux of the hydrophobic M-SS, 0 h/FAS of 33 kg/m^2·h, is higher than all the omniphobic M-SS HFMs prepared at different reaction times. As for the omniphobic M-SS HFMs, the initial vapour flux of the M-SS, 1 h/FAS, M-SS, 2 h/FAS, M-SS, 3 h/FAS and M-SS, 5 h/FAS, was 32.3, 31, 30 and 32.6 kg/m^2·h respectively higher than the M-SS, 4 h/FAS of 28.8 kg/m^2·h. This difference in the vapour fluxes could be ascribed to the difference in the surface roughness of the omniphobic HFMs, which resulted from different hydrothermal reaction times. The lowest initial vapour flux observed at the M-SS, 4 h/FAS, could be due to its lower surface pores size and porosity. This observation is consistent with Woo et al. [60] findings, which reported that membranes with higher roughness usually show lower permeation flux due to increased vapour transfer resistance. However, the highest initial vapour flux observed at the M-SS, 5 h/FAS, can be attributed to the cracks formed on the omniphobic layer, which increased the vapour permeation to the cold permeate side, as seen in Fig. 5F.

Table 3
Membrane mass before and after the hydrothermal step.

Membrane code	Membrane mass (g)		Mass different (g)	Mass different (%)
	Before hydrothermal step	After hydrothermal step		
M-SS,1 h/FAS	0.1320 ± 1.2	0.1395 ± 0.9	0.0075	5.4
M-SS, 2 h/FAS	0.1318 ± 1.3	0.1450 ± 2.1	0.0132	9.1
M-SS, 3 h/FAS	0.1319 ± 0.8	0.1486 ± 1.4	0.0167	11.2
M-SS, 4 h/FAS	0.1321 ± 0.5	0.1509 ± 0.7	0.0188	12.5
M-SS, 5 h/FAS	0.1320 ± 1.0	0.1507 ± 0.6	0.0187	12.4

Table 4
ICP-OES results after ultrasonication in the Milli-Q water for 30 min.

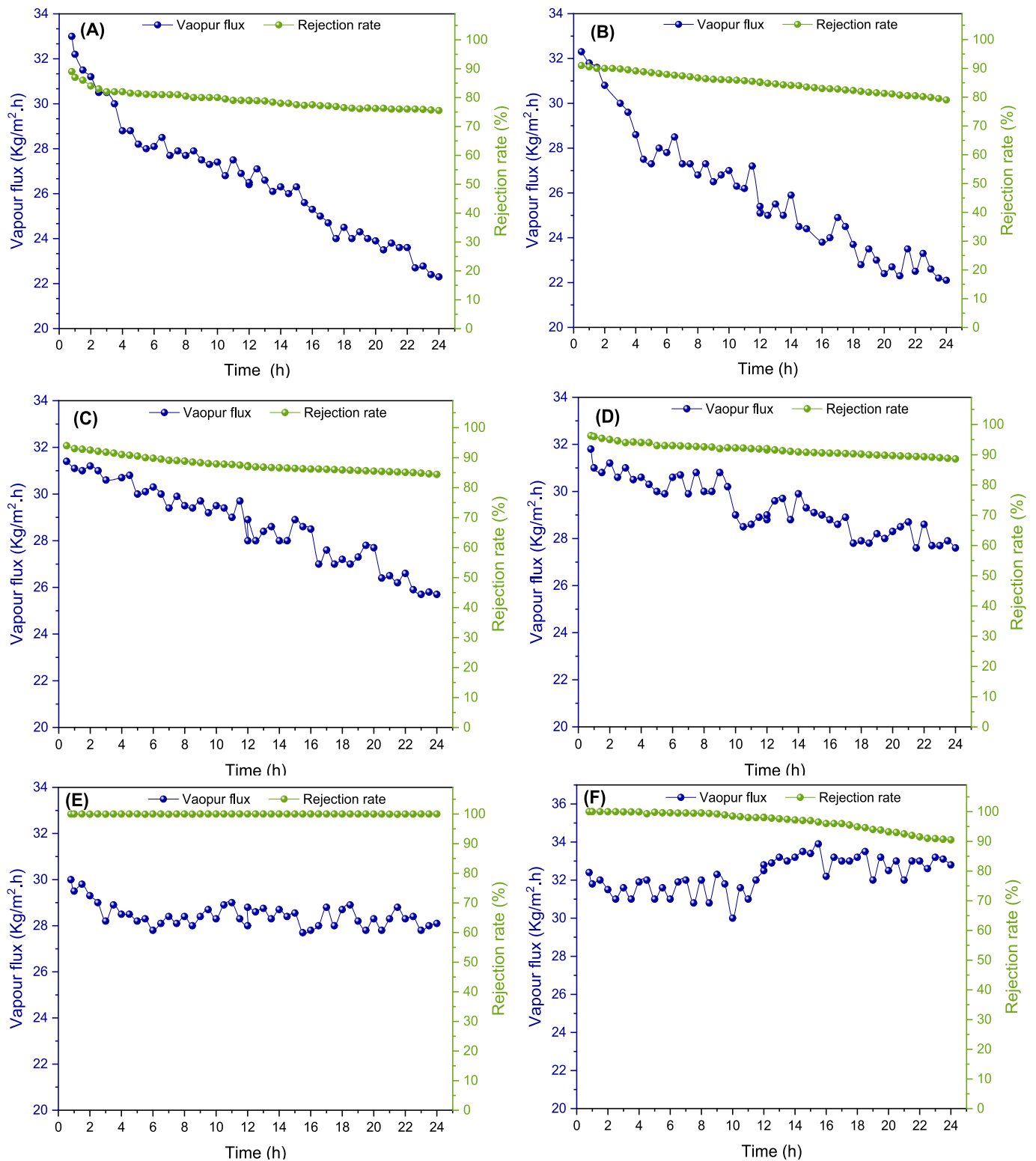| Membrane code	Concentration level of Cu (mg/L)			
	Replicates			
	1	2	3	Average
M-SS, 1 h/FAS	5.4521	6.2789	6.0234	5.9181
M-SS, 2 h/FAS	5.2178	5.0237	5.1986	5.1467
M-SS, 3 h/FAS	1.9832	0.9986	1.8964	1.6260
M-SS, 4 h/FAS	0	0	0	0
M-SS, 5 h/FAS	0.0016	0.0001	0.0009	0.0008

Fig. 14. The effect of time on vapour flux and salt rejection performance of (A) hydrophobic M-SS, 0 h/FAS, (B) M-SS,1 h/FAS, (C) M-SS,2 h/FAS, (D) M-SS,3 h/FAS (E) M-SS,4 h/FAS and (F) M-SS,5 h/FAS at feed solution of 35 g/L NaCl of and 10 mg/L humic acid for 24 h MD operation [T_{feed}: 80 °C].

A sharp decrease with unstable vapour flux is observed for the hydrophobic M-SS, 0 h/FAS and M-SS,1 h/FAS, during the initial 10 h. This observation could be linked to the quick NaCl crystals and humic acid accumulation on the membrane surface as a foulant layer, as evidenced by the colour change and thin layer formation on the surfaces of HFMs (see Fig. 15Ai-Bi), which increased the vapour permeation resistance and the membrane hydrophilicity because of carboxylic and hydroxyl functional groups of the accumulated humic acid as the fouling layer [61]. The current result is in line with the outcomes of Bush et al. [61], who reported that the existence of humic acid decreases MD vapour flux due to the foulant layer formation on the membrane surface, which usually increments the hydraulic resistance and the heat transfer

resistance, reducing the membrane driving force (vapour pressure) [62,63]. In addition, the unstable vapour flux is observed for hydrophobic M-SS, 0 h/FAS and M-SS,1 h/FAS M-SS until the end of the MD process with an obvious reduction in the salt rejection performance to about 53 and 62 %, respectively. As for the hydrophobic M-SS, 2 h/FAS and M-SS,3 h/FAS M-SS, a gradual reduction and unstable vapour flux and salt rejection performance were observed until the end of the process (100 h) (see Fig. 15(Ci-Di)). The unstable behaviour could be ascribed to the heterogeneous pore size distributions, which impacted the liquid entry pressure distribution due to the irregular thickness fouling layer formation on the membrane surface. This outcome was consistent with the post-fouling SEM images in Fig. 15(Ai-Di). In comparison, the omniphobic HFMs at M-SS, 3 h/FAS, M-SS,4 h/FAS and M-SS,5 h/FAS show more stable vapour flux of 30, 28.8 and 32.6 kg/m^2·h with lower reduction in salt rejection performance of 89.06, 99.99 and 91.98 %, respectively.

The most stable vapour flux is observed at M-SS,4 h/FAS (28.8 kg/m^2·h), with almost no obvious vapour flux reduction and no conductivity increment in the permeate stream through the MD operation (see Fig. 16). In addition, no fouling layer on the membrane surface is observed with no colour change on the membrane surface, as evidenced in Fig. 15(Ei). This observation could be due to the high membrane omniphobocity and contact angles against all liquid drops, as shown in Figs. 11E and 13E, making it the most suitable omniphobic membrane for the MD process among all tested omniphobic HFMs. This result also proves its high omniphobocity by reducing the interaction between the membrane surface and the foulant, preventing the accumulation of foulant on the membrane surface. As for the M-SS,5 h/FAS, a slight increase in vapour flux and reduced salt rejection performance are noted (Fig. 15Fi), attributing to cracks obtained on the membrane surface (see Fig. 5F). The crakes on the membrane surface increase the vapour permeation, and the permeation of some liquid drops to the cold
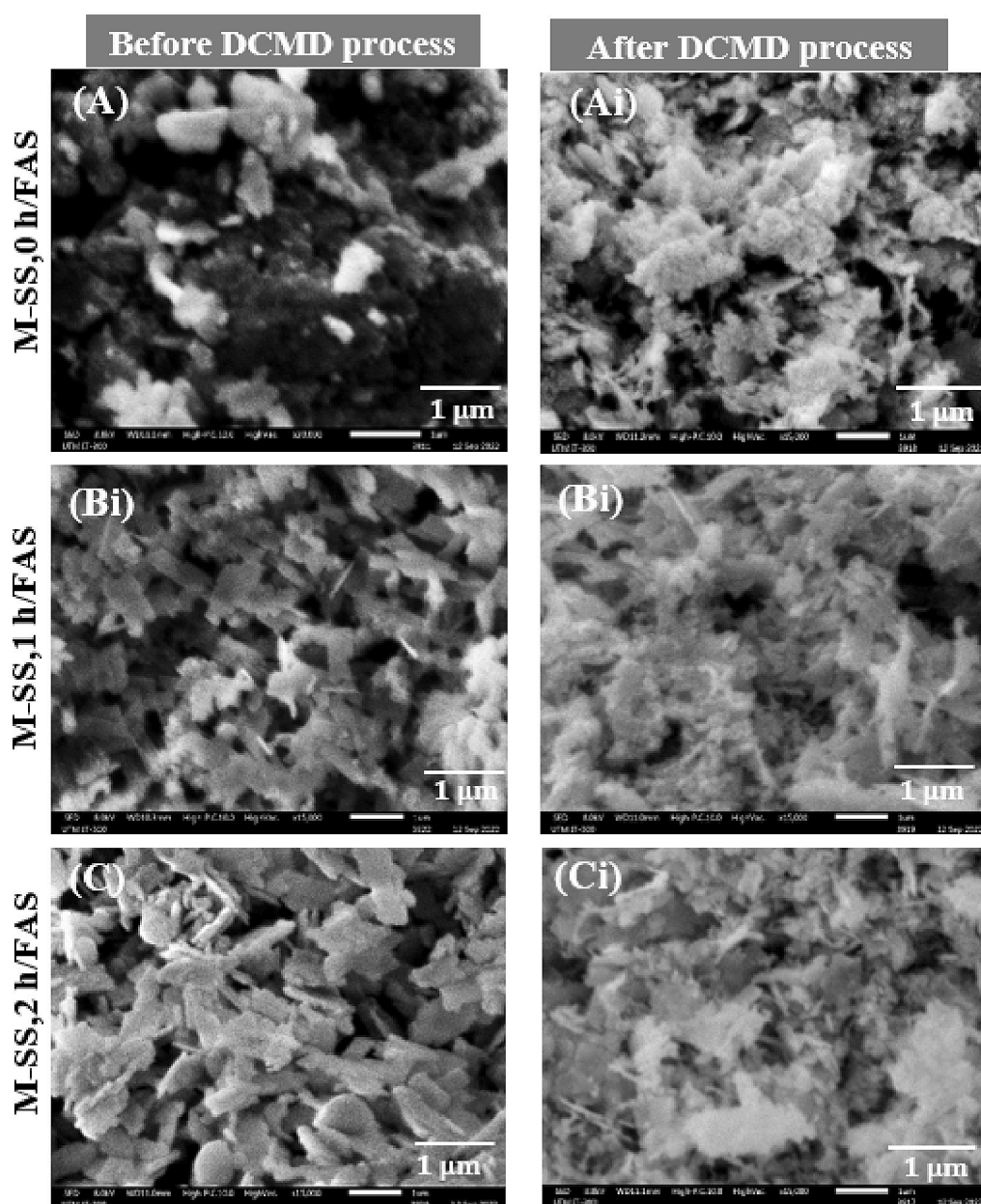

Fig. 15. SEM images of the membrane surface before (left images) and after (right images) MD operations of (A) M-SS,0 h/FAS, (B) M-SS,1 h/FAS, (C) M-SS,2 h/FAS (D) M-SS,3 h/FAS, (E) M-SS,4 h/FAS and (F) M-SS,5 h/FAS with a feed solution of 35 g/L NaCl of and 10 mg/L humic acid for 24 h MD operation.
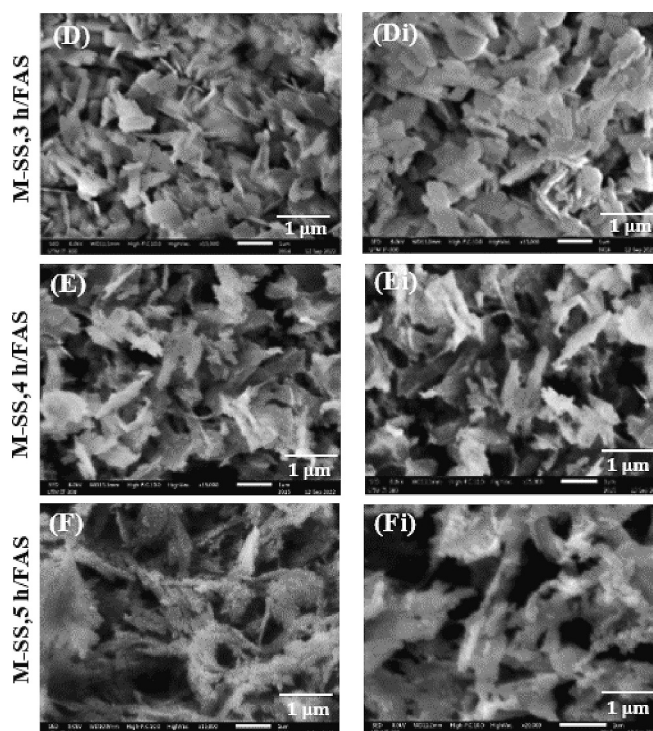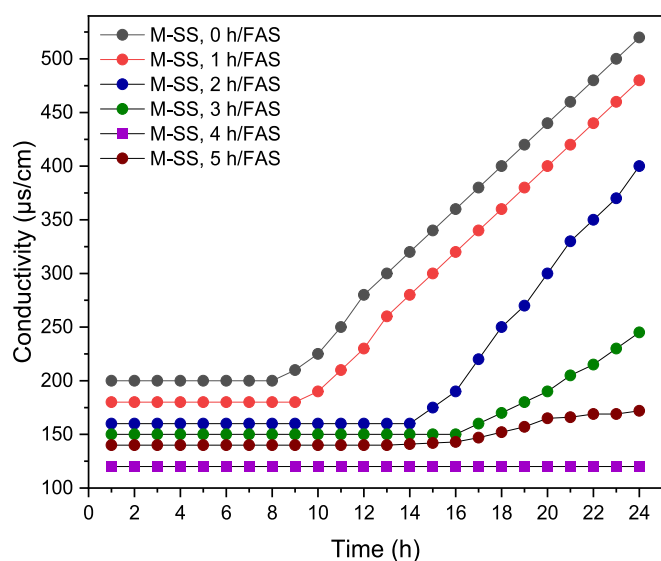
Fig. 15. (*continued*).

Fig. 16. Conductivity of M-SS, 0 h/FAS, M-SS,1 h/FAS, M-SS,2 h/FAS, M-SS,3 h/FAS, M-SS,4 h/FAS and M-SS,5 h/FAS for 24 h (Feed solution of 35 g/L NaCl and 10 mg/L humic acid).

permeate side increases the permeate conductivity, as evidenced in Fig. 16. The permeated salt increases the conductivity, as reported in works in the literature [7,20]. In contrast, foulants accumulation on the membrane surface increased vapour transport resistance and reduced flux. The attachment of foulant on the membrane surface leads to partial pore blockage resulting in higher resistance towards mass transport and limiting the amount of vapour to pass through the membrane pores affecting membrane separation performance [64]. However, the omniphobic mullite-SS HFM with leaf-like surface structure at 4 h hydrothermal reaction time showed the most stable permeate flux at an average flux of 28.4 kg/m^2·h, a salt rejection rate of 99.99 % and with

almost no fouling deposition on the membrane surface among other omniphobic HFMs, as evidenced in Figs. 14 and 15.

Fig. 16 shows a low conductivity for all modified HFMs based on the hydrothermal reaction time at the initial permeate. This decline can be attributed to the surface modification of the membrane by the FAS treatment due to a deposited thin layer of CuO nanoparticles on the membrane surface. This modification alters the charge and hydrophilicity of the membrane, making it less favourable for ion adsorption and reducing ion conductivity. The deposition of the CuO nanoparticles also acts as a barrier, impeding the passage of ions through the membrane and decreasing permeate conductivity. The selective ion transport properties of CuO nanoparticles allow them to block ions while allowing water molecules to pass through. As a result, the altered surface characteristics contribute to a decrease in initial permeate conductivity. Besides, forming CuO nanoparticles on the membrane surface enhances the rejection of charged species in the feed solution. The CuO layer acts as a physical barrier and repels ions, reducing their presence in the permeate stream and lowering conductivity. It is important to note that the decrease in initial permeate conductivity may vary depending on the specific properties of the feed solution, such as ion concentration and type. Different ions may exhibit varying affinities for the CuO layer, resulting in different degrees of conductivity reduction. An increase in conductivity was observed at different time intervals 9 min for M-SS, 0 h/FAS and M-SS, 1 h/FAS, 14 min for M-SS, 2 h/FAS and 16 min for M-SS, 3 h/FAS and M-SS, 5 h/FAS. This increase can be attributed to fouling accumulation on the membrane surface, allowing some salt to permeate to the permeate side. However, no change in conductivity was observed for M-SS, 4 h/FAS, indicating high fouling and wetting resistance on the membrane surface.

The hydrophobic and all omniphobic HFMs were also analyzed by the EDX after the DCMD process to examine the foulant accumulation (post-foulant) on the surfaces of membranes, as depicted in Table 5 (M-SS,0–5 h/FAS) and Fig. 17(A–F). Compared to the EDX analysis in Table 1 and Fig. 7 before the MD process, new elements such as nitrogen (N, light blue), which is attributed to humic acid, chloride (Cl, light red) and sodium (Na, dark red) which attributed to the NaCl crystals were

Table 5
Elemental composition on the surface of all modified mullite-SS HFMs after MD.

Membrane code	Elements content (wt%) in the membrane surface										
	Si	Al	Cu	F	O	Fe	Cr	Ni	Na	Cl	N
M-SS,0 h/FAS	9.9	9.7	–	5.8	40.1	6.2	1.5	0.8	3.8	2.6	1.7
M-SS,1 h/FAS	9.5	9.4	6.7	5.0	39.5	6.7	1.6	0.9	1.6	1.8	0.8
M-SS, 2 h/FAS	12.7	11.8	6.0	5.8	43.1	6.8	1.8	0.8	0.8	0.7	0.5
M-SS, 3 h/FAS	11.3	12.0	18.0	6.1	32.0	6.7	1.8	0.8	0.3	0.2	0.3
M-SS, 4 h/FAS	6.8	7.4	28.2	6.0	34.8	4.8	1.3	0.3	0.0	0.0	0.0
M-SS, 5 h/FAS	8.2	4.6	26.7	3.1	34.9	4.8	0.9	0.3	0.0	0.0	0.1

Note: Si: silicon; Al: aluminium; Cu: copper; F: fluorine; O: oxygen; Fe: iron; Cr: chromium; Ni: nickel; Na: sodium; Cl: chloride; N: nitrogen.

found on the surfaces of all HFMs with no increase in the carbon (C, dark brown) concentration. The deposition of these elements indicates the NaCl and humic acid fouling layer formation on omniphobic HFMs. Hydrophobic M-SS, 0 h/FAS, shows the highest concentrations of N, Cl and Na concentration with 1.17, 2.60 and 3.80 % (w/w), respectively, on the membrane surface (see Table 5 (M-SS,0 h/FAS)). Membranes of M-SS,1 h/FAS, M-SS,2 h/FAS and M-SS,3 h/FAS contain lower N, Cl and Na concentrations than the hydrophobic HFM (Table 5 (M-SS,1–3 h/FAS)). This observation is consistent with the results shown in Fig. 17 (A–D). However, at M-SS, 5 h/FAS, no Cl and Na are obtained on the membrane surface, while the N element presents with a very low concentration of 0.1 % (w/w) (see Table 5 (M-SS,5 h/FAS)). The presence of the N element indicates the attachment of some humic acid on the membrane surface (fouling). But the amount is much lower than most membranes with shorter hydrothermal reaction time (i.e., 0, 1, 2 and 3) due to its better omniphobicity. As for M-SS,4 h/FA, no N, Cl and Na elements are found on the membrane surface, as demonstrated in Table 5 (M-SS,4 h/FAS), attributing its high omniphobicity, self-cleaning and strong liquid drops rejection tendency. The outcome is attributed to the excellent growth of the leaf-like on the membrane surface, as evident in Fig. 5E, and the presence of the FAS agent, which reduced the membrane surface energy to an ultra-low level. As a result, the foulants in the feed solution have low interaction with the membrane surface and do not attach to the membrane surface.

The other significant observation is that the concentration of the Cu element (dark purple) on the surfaces of M-SS,1 h/FAS (6.7 % (w/w)), M-SS,2 h/FAS (6.0 % (w/w)) and M-SS,3 h/FAS (18 % (w/w)) is lower after the MD process compared to its concentration before MD process of 13.6, 14,5 and 22.5 % (w/w), respectively (see Table 5). The reduction in the Cu concentration could be ascribed to the loss of some of the omniphobic layer during the MD process (see Fig. 17(A–C)) or denser foulant layers formation on the surfaces of membranes. However, the Cu concentration after the MD process for M-SS,4 h/FAS (28.2 % (w/w)) and M-SS,5 h/FAS (26.7 % (w/w)) was very close to its concentration before the MD process of 25.2 and 24.9 % (w/w), respectively. This note could be due to the excellent stability of the omniphobic layers on the surfaces of the membranes and the self-cleaning property. This observation is also consistent with the results presented in Fig. 17(E–F).

The performance of the hydrophobic and omniphobic mullite-SS HFMs against wetting issues was also evaluated. The findings are presented in Table 6 based on the contact angle measurement of DI water, olive oil and ethanol before and after the DCMD process. There was an obvious reduction in the contact angle measurements before and after the DCMD process at M-SS, 1 h/FAS, M-SS, 2 h/FAS, M-SS and 3 h/FAS, attributing to the effect of their omniphobic layers by foulants accumulation in the feed solution. The attachment of foulants on the membrane surface increases the surface energy of the membrane surface. The reduction in the contact angles indicates wetting issues on the membrane surface. At the M-SS, 5 h/FAS, the change in the contact angle values of all liquids was less compared to omniphobic membranes prepared at 1, 2, and 3 h. In contrast, at M-SS, 4 h/FAS, there was a slight change in the contact angle measurements observed for DI water, olive oil and ethanol after the DCMD process, where the values of the contact

angles reduced from 167.2°, 145.8° and 144.8° to 166.3°,144.4° and 142.4 respectively. The declining percentage of the contact angle values of DI water and olive oil was less than 1 %, while ethanol was 1.66 %, indicating the high wetting resistance of the omniphobic M-SS, 4 h/FAS HFM.

Table 7 shows the separation performance and the contact angle of the optimum omniphobic mullite-SS HFMs prepared at 4 h hydrothermal reaction time compared to the other omniphobic CHFMs reported in the literature. In this study, the preparation of the omniphobic layer by CuO nanoparticles using the hydrothermal technique required a reaction time ranging from 1 to 5 h, which was considerably low compared to the omniphobic mullite HFM prepared by cobalt oxide (Co_3O_4) nanoparticles using the same technique which ranged from 10 to 19 h [21]. The water flux and contact angles of the omniphobic M-SS, 4 h/FAS HFM prepared by CuO nanoparticles obtained in this study were significantly higher than those prepared by the hydrothermal reaction technique reported in previous works using mullite materials (see Table 7). The water and oil contact angles of 167° and 152°, respectively, were higher than that of omniphobic HFMs prepared by TiO_2, ZnO and Co_3O_4 nanoparticles exhibited in Table 7. The membrane also showed a high rejection performance of up to 99.99 %. This indicates that the mullite-SS 4 h/FAS can achieve good flux and rejection performance even at high salt concentrations and feed temperatures.

4. Conclusion

Mullite-SS HFM surface was successfully modified to the omniphobic properties using CuO nanoparticles as a surface activator via hydrothermal technique at different hydrothermal reaction times (i.e., 1, 2, 3, 4 and 5 h) and fluorination by FAS (C8) as a surface energy agent. Successful deposition of CuO nanoparticles was observed on the surfaces of the HFMs with different surface roughness levels, which strongly depended on the hydrothermal reaction times achieved. The improvement in the surface roughness by the CuO nanoparticles was observed with the increasing hydrothermal reaction times from 1 to 4 h. The optimum membrane roughness with a leaf-like structure was observed at the M-SS, 4 h/FAS HFM. After a 5 h hydrothermal reaction, several defects and cracks were observed on the membrane surface, as evidenced in the SEM images. The impact of the CuO roughness and FAS (C8) fluorination on the wetting properties of all modified HFMs was evaluated by measuring LEP and contact angles of water, olive oil and ethanol and compared with hydrophobic HFM. Different values of LEP and contact angles of water, olive oil and ethanol were observed between all omniphobic HFMs and hydrophobic HFM. The hydrophobic HFM demonstrated the lowest contact angle values for all liquids used in this test, while the omniphobic HFM prepared at 4 h/FAS exhibited superomniphobic properties with high contact angles for water (167°), olive oil (146°) and omniphobic properties towards ethanol (144°) because of the dual functions of re-entrant structure and fluorination on the membrane surface. This omniphobic membrane also showed a high vapour flux of 29 kg/m^2.h and a high rejection performance of up to 99.99 % at a feed temperature of 80 °C.
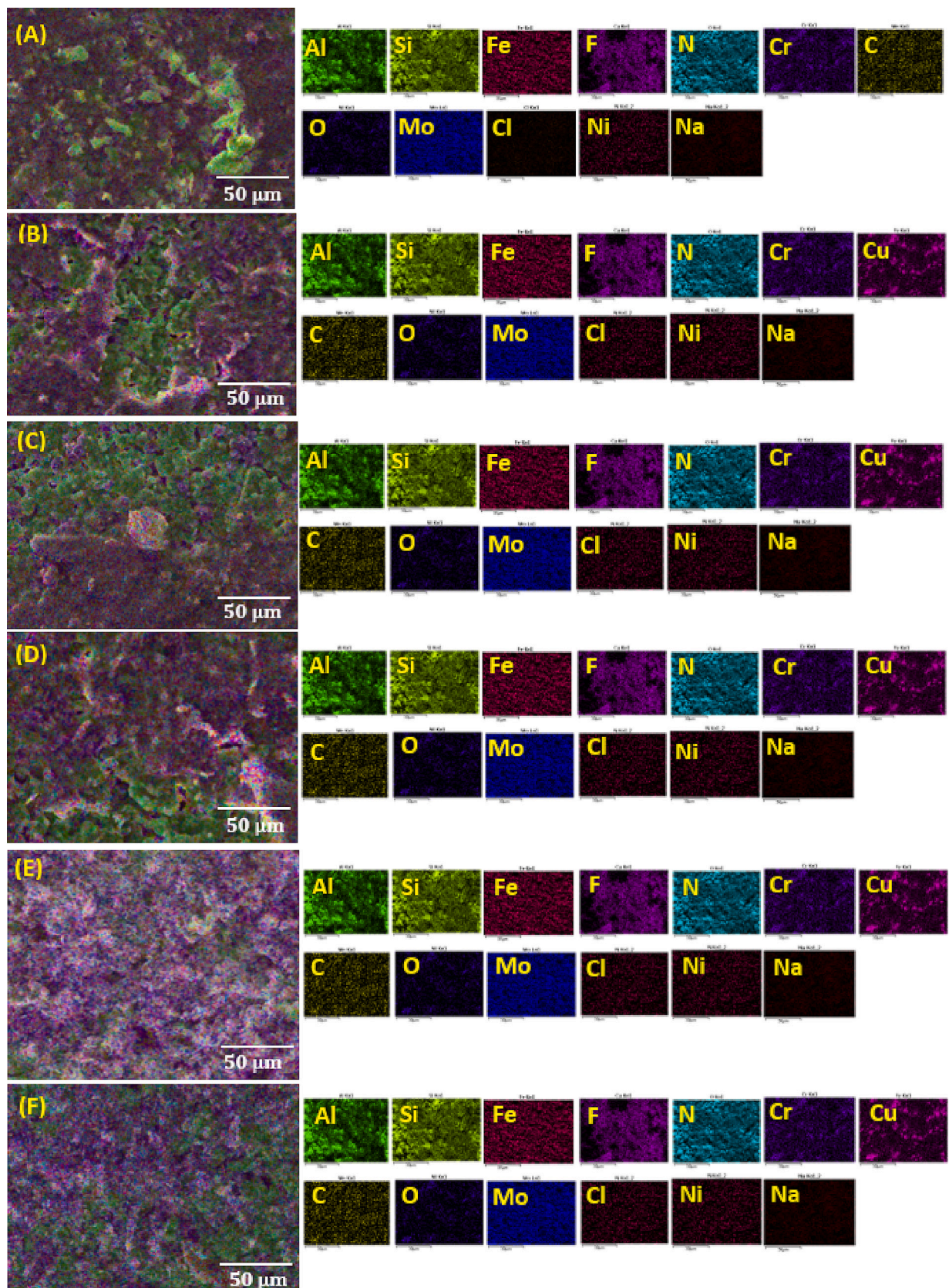
Fig. 17. EDX analysis on the top cross-section of (A) hydrophobic M-SS, 0 h/FAS and omniphobic HFMs of (B) M-SS, 1 h/FAS, (C) M-SS, 2 h/FAS, (D) M-SS, 3 h/FAS and (E) M-SS, 4 h/FAS and (F) M-SS,5 h/FAS.

Table 6

Contact angles of hydrophobic and omniphobic M-SS HFMs prepared at different hydrothermal reaction times before and after 24 h DCMD operation [error bars are based on standard errors from three duplicate calculations].

Membrane code	Contact angles before DCMD			Contact angles after DCMD			Difference (%)		
	DI water	Olive oil	Ethanol	DI water	Olive oil	Ethanol	DI water	Olive oil	Ethanol
M-SS, 0 h/FAS	133.0 ± 2.2	25.2 ± 1.2	22.2 ± 3.1	109.2 ± 2.3	16.4 ± 1.9	11.9 ± 1.8	17.89	34.92	46.39
M-SS, 1 h/FAS	141.0 ± 2.3	99.9 ± 1.8	70.2 ± 1.8	115.9 ± 3.2	69.8 ± 1.9	35.9 ± 2.0	17.80	30.13	48.86
M-SS, 2 h/FAS	149.1 ± 2.7	119.1 ± 1.1	100.8 ± 2.1	121.0 ± 1.6	98.6 ± 2.4	69.6 ± 3.1	18.85	17.21	30.95
M-SS, 3 h/FAS	155.0 ± 3.1	133.0 ± 2.1	128.9 ± 1.7	139.9 ± 2.2	120.8 ± 4.0	116.0 ± 2.2	9.74	9.17	10.0
M-SS, 4 h/FAS	167.2 ± 1.0	145.8 ± 1.6	144.8 ± 1.1	166.3 ± 2.0	144.4 ± 3.1	142.4 ± 1.2	0.54	0.96	1.66
M-SS, 5 h/FAS	159.1 ± 2.0	142.2 ± 1.8	136.2 ± 1.4	147.2 ± 2.1	130.7 ± 1.5	120.6 ± 1.3	7.50	8.09	11.45

Table 7

Comparison of the separation performance and contact angles obtained in this study with other omniphobic ceramic membranes reported in the literature.

Membrane material	Surface modification/structure	Contact angle (°)	Operation temperatures (°C) feed/permeate	Separation performance			Ref.
				Feed composition	Flux (kg/m²·h)	Rejection (%)	
Al_2O_3	ZnO/FAS 17/nanorod & nanoparticle	Water ~152.8 Ethanol ~110.3	70/15	NaCl (1.0 M)/SDS (2.0 mM)	14	99.99	[65]
Silica sand	SiNPs/FAS/PVDF spherical-like	Water ~167 Red palm oil ~157 Ethanol ~146	70/20	NaCl (35 g/L)/HA (10 mg/L)	44.8	99.99	[20]
Mullite-ball clay	TiO_2/FAS (C8) micro-flowers	Ethylene glycol ~150 Olive oil ~140	65/20	NaCl (0.5 M)/HA (10 mg/L)	4	99.99	[7]
Mullite-kaolinite	Co_3O_4/FAS17 spider web-like	Water ~165 Olive oil ~142 Engine oil ~154	70/20	NaCl (0.5 M)/HA (8 mg/L)	22.5	99.99	[21]
Mullite-kaolinite/SS	CuO/FAS C8 leaf-like	Water ~167 Olive oil ~146 Ethanol ~144	80/10	NaCl (35 g/L)/HA (10 mg/L)	29	99.99	This study

Note: Humic acid (HA); Sodium dodecyl sulfate (SDS); Sodium chloride (NaCl); Cobalt oxide (Co_3O_4); Fluoroalkylsilane (FAS).

Declaration of competing interest

The authors declare that they have no known competing financial interests or personal relationships that could have appeared to influence the work reported in this paper.

Data availability

No data was used for the research described in the article.

References

[1] W.A.F.W. AbdulKadir, A.L. Ahmad, O.B. Seng, N.F.C. Lah, Biomimetic hydrophobic membrane: a review of anti-wetting properties as a potential factor in membrane development for membrane distillation (MD), J. Ind. Eng. Chem. 91 (2020) 15–36.

[2] K.-J. Lu, T.-S. Chung, Membrane Distillation: Membranes, Hybrid Systems and Pilot Studies, CRC Press, 2019.

[3] N.M.A. Omar, et al., Bottlenecks and recent improvement strategies of ceramic membranes in membrane distillation applications: a review, J. Eur. Ceram. Soc. 42 (2022) 5179–5194.

[4] Z. Wang, Fouling and Wetting in Membrane Distillation: Mechanisms and Mitigation Strategies, Vanderbilt University, 2018.

[5] N.M.A. Omar, et al., Recent progress, bottlenecks, improvement strategies and the way forward of membrane distillation technology for arsenic removal from water: a review, J. Water Process Eng. 52 (2023), 103504.

[6] T. Subrahmanya, et al., High performance self-heated membrane distillation system for energy efficient desalination process, J. Mater. Chem. A 9 (12) (2021) 7868–7880.

[7] M.H. Abd Aziz, et al., Enhanced omniphobicity of mullite hollow fiber membrane with organosilane-functionalized TiO2 micro-flowers and nanorods layer deposition for desalination using direct contact membrane distillation, J. Membr. Sci. 607 (2020), 118137.

[8] D. Sivaraj, K. Vijayalakshmi, M. Srinivasan, P. Ramasamy, Graphene oxide reinforced bismuth titanate for photocatalytic degradation of azo dye (DB15) prepared by hydrothermal method, Ceram. Int. 47 (17) (2021) 25074–25080.

[9] E. Velayi, R. Norouzbeigi, Single-step prepared hybrid ZnO/CuO nanopowders for water repellent and corrosion resistant coatings, Ceram. Int. 45 (14) (2019) 16864–16872.

[10] C.-L. Xu, F. Song, X.-L. Wang, Y.-Z. Wang, Surface modification with hierarchical CuO arrays toward a flexible, durable superhydrophobic and self-cleaning material, Chem. Eng. J. 313 (2017) 1328–1334.

[11] Z. She, Q. Li, Z. Wang, L. Li, F. Chen, J. Zhou, Novel method for controllable fabrication of a superhydrophobic CuO surface on AZ91D magnesium alloy, ACS Appl. Mater. Interfaces 4 (8) (2012) 4348–4356.

[12] M. Aijaz, et al., Recent Progress, challenges, and opportunities of membrane distillation for heavy metals removal, Chem. Rec. 22 (2022) 1–30.

[13] S. Lin, S. Nejati, C. Boo, Y. Hu, C.O. Osuji, M. Elimelech, Omniphobic membrane for robust membrane distillation, Environ. Sci. Technol. 1 (11) (2014) 443–447.

[14] A.K. Kota, G. Kwon, A. Tuteja, The design and applications of superomniphobic surfaces, NPG Asia Mater. 6 (7) (2014) 1–16.

[15] Y. Cheng, S. Lu, W. Xu, K. Cao, J. Li, Y. Zheng, Controllable fabrication of superhydrophobic alloys surface on copper substrate for self-cleaning, anti-icing, anti-corrosion and anti-wear performance, Surf. Coat. Technol. 333 (2018) 61–70.

[16] N. Xu, D.K. Sarkar, X.G. Chen, H. Zhang, W. Tong, Superhydrophobic copper stearate/copper oxide thin films by a simple one-step electrochemical process and their corrosion resistance properties, RSC Adv. 6 (42) (2016) 35466–35478.

[17] W. Jiang, W. He, F. Xiao, S. Yuan, H. Lu, B. Liang, Preparation and antiscaling application of superhydrophobic anodized CuO nanowire surfaces, Ind. Eng. Chem. Res. 54 (27) (2015) 6874–6883.

[18] L. Chen, Z. Guo, W. Liu, Outmatching superhydrophobicity: bio-inspired re-entrant curvature for mighty superamphiphobicity in air, J. Mater. Chem. A 5 (28) (2017) 14480–14507.

[19] N.M.A. Omar, Mohd Hafiz Dzarfan Othman, Zhong Sheng Tai, Mohd Hafiz Puteh, Juhana Jaafar, Mukhlis A. Rahman, Ahmad Fauzi Ismail, Keng Yinn Wong, Effect of sintering temperature on functional properties of mullite-kaolinite and stainless steel composed hollow fibre membrane for oil-in-water emulsion separation, J. Taiwan Inst. Chem. Eng. 146 (2023).

[20] S.A. Alftessi, et al., Omniphobic surface modification of silica sand ceramic hollow fiber membrane for desalination via direct contact membrane distillation, Desalination 532 (2022), 115705.

[21] M.F. Twibi, et al., Novel approach to surface functionalization of mullite-kaolinite hollow fiber membrane using organosilane-functionalized Co3O4 spider web-like layer deposition for desalination using direct contact membrane distillation, Ceram. Int. 48 (14) (2022) 21025–21036.

[22] T. Wang, Y. Yun, M. Wang, C. Li, G. Liu, W. Yang, Superhydrophobic ceramic hollow fiber membrane planted by ZnO nanorod-array for high-salinity water desalination, J. Taiwan Inst. Chem. Eng. 105 (2019) 17–27.

[23] Z. Li, Z. Li, C. Zuo, X. Fang, Application of nanostructured TiO2 in UV photodetectors: a review, Adv. Mater. 34 (28) (2022) 2109083.

[24] M. Al-Mamun, S. Kader, M. Islam, M. Khan, Photocatalytic activity improvement and application of UV-TiO2 photocatalysis in textile wastewater treatment: a review, J. Environ. Chem. Eng. 7 (5) (2019), 103248.

[25] A.S. Nur, et al., A review on the development of elemental and codoped TiO2 photocatalysts for enhanced dye degradation under UV–vis irradiation, J. Water Process Eng. 47 (2022), 102728.

[26] C. Chen, B. Wang, H. Liu, T. Chen, H. Zhang, J. Qiao, Synthesis of 3D dahlia-like Co3O4 and its application in superhydrophobic and oil-water separation, Appl. Surf. Sci. 471 (2019) 289–299.

[27] A. Ivanets, et al., Preparation and properties of microfiltration membranes based on natural crystalline SiO2, Ceram. Int. 40 (8) (2014) 12343–12351.

[28] J. Li, et al., Preparation of omniphobic PVDF membranes with silica nanoparticles for treating coking wastewater using direct contact membrane distillation: electrostatic adsorption vs. chemical bonding, J. Membr. Sci. 574 (2019) 349–357 (2019/03/15/), https://doi.org/10.1016/j.memsci.2018.12.079 (2019/03/15/).

[29] T. Phoo-ngernkham, P. Chindaprasirt, V. Sata, S. Hanjitsuwan, S. Hatanaka, The effect of adding nano-SiO2 and nano-Al2O3 on properties of high calcium fly ash geopolymer cured at ambient temperature, Mater. Des. 55 (2014) 58–65.

[30] J. Ren, J. Li, Z. Xu, Y. Liu, F. Cheng, Simultaneous anti-fouling and flux-enhanced membrane distillation via incorporating graphene oxide on PTFE membrane for coking wastewater treatment, Appl. Surf. Sci. 531 (2020), 147349 (2020/11/30/), https://doi.org/10.1016/j.apsusc.2020.147349 (2020/11/30/).

[31] N. Sun, et al., Insights into the enhanced flux of graphene oxide composite membrane in direct contact membrane distillation: the different role at evaporation and condensation interfaces, Water Res. 212 (2022), 118091 (2022/04/01/), https://doi.org/10.1016/j.watres.2022.118091 (2022/04/01/).

[32] J.Y. Lim, N. Mubarak, E. Abdullah, S. Nizamuddin, M. Khalid, Recent trends in the synthesis of graphene and graphene oxide based nanomaterials for removal of heavy metals—a review, J. Ind. Eng. Chem. 66 (2018) 29–44.

[33] L.-H. Chen, et al., Nanostructure depositions on alumina hollow fiber membranes for enhanced wetting resistance during membrane distillation, J. Membr. Sci. 564 (2018) 227–236.

[34] A. Changdar, S.S. Chakraborty, Laser processing of metal foam-a review, J. Manuf. Process. 61 (2021) 208–225.

[35] K. Choy, Chemical vapour deposition of coatings, Prog. Mater. Sci. 48 (2) (2003) 57–170.

[36] A. Kumar, N. Yadav, M. Bhatt, N.K. Mishra, P. Chaudhary, R. Singh, Sol-gel derived nanomaterials and it's applications: a review, Res. J. Chem. Sci. 2231 (2015) 606X (ISSN).

[37] G. Zhao, et al., Sprayed separation membranes: a systematic review and prospective opportunities, Green Energy Environ. 7 (2022) 1143–1160.

[38] A.A. Leonardi, M.J.L. Faro, A. Irrera, Silicon nanowires synthesis by metal-assisted chemical etching: a review, Nanomaterials 11 (2) (2021) 383.

[39] J.-W. Wang, et al., Porous β-sialon planar membrane with a robust polymer-derived hydrophobic ceramic surface, J. Membr. Sci. 535 (2017) 63–69.

[40] X. Zhong, H. Hu, L. Yang, J. Sheng, H. Fu, Robust hyperbranched polyester-based anti-smudge coatings for self-cleaning, anti-graffiti, and chemical shielding, ACS Appl. Mater. Interfaces 11 (15) (2019) 14305–14312.

[41] Z. Lv, S. Yu, K. Song, X. Zhou, X. Yin, Fabrication of a leaf-like superhydrophobic CuO coating on 6061Al with good self-cleaning, mechanical and chemical stability, Ceram. Int. 46 (10) (2020) 14872–14883.

[42] M.A. Khan, N. Nayan, M.K. Ahmad, C.F. Soon, Surface study of CuO nanopetals by advanced nanocharacterization techniques with enhanced optical and catalytic properties, Nanomaterials 10 (7) (2020) 1298.

[43] C. Cao, F. Wang, M. Lu, Superhydrophobic CuO coating fabricated on cotton fabric for oil/water separation and photocatalytic degradation, Colloids Surf. A Physicochem. Eng. Asp. 601 (2020), 125033.

[44] A.C. Fernandez, J. Jesudurai, Hydrothermal synthesis and characterization of copper oxide flower-likeNanostructures, Elixir Nanocompos. Mater. 50 (2012) 10541–10543.

[45] A. Sezavar, S.A. Sajjadi, A. Babakhani, R.L. Peng, K. Yuan, Oxidation behavior of a nanostructured compositionally graded layer (CGL) thermal barrier coating (TBC) deposited on IN-738LC, Surf. Coat. Technol. 374 (2019) 374–382.

[46] S. T.M, et al., Flow-through in-situ evaporation membrane enabled self-heated membrane distillation for efficient desalination of hypersaline water, Chem. Eng. J. 452 (2023), 139170 (2023/01/15/), https://doi.org/10.1016/j.cej.2022.139170 (2023/01/15/).

[47] N.M.A. Omar, et al., Fabrication and characterization of a novel mullite-stainless steel composed hollow fibre membrane for oil/water separation, Ain Shams Eng. J. 7 (2023) 102260–102279.

[48] J. Weber, Y. Chen, E. Jamroz, T. Miano, Preface: humic substances in the environment, J. Soils Sediments 18 (8) (2018) 2665–2667.

[49] J. Weber, Humic substances and their role in the environment, EC Agric. 3 (2020).

[50] J. Jeevahan, M. Chandrasekaran, G. Britto Joseph, R. Durairaj, G. Mageshwaran, Superhydrophobic surfaces: a review on fundamentals, applications, and challenges, J. Coat. Technol. Res. 15 (2) (2018) 231–250.

[51] Y.O. Raji, et al., Optimization of a high-performance poly (diallyl dimethylammonium chloride)-alumina-perfluorooctanoate intercalated ultrafiltration membrane for treating emulsified oily wastewater via response surface methodology approach, Membranes 11 (12) (2021) 956.

[52] J. Zuo, S. Bonyadi, T.-S. Chung, Exploring the potential of commercial polyethylene membranes for desalination by membrane distillation, J. Membr. Sci. 497 (2016) 239–247.

[53] K.-J. Lu, J. Zuo, T.-S. Chung, Novel PVDF membranes comprising n-butylamine functionalized graphene oxide for direct contact membrane distillation, J. Membr. Sci. 539 (2017) 34–42.

[54] N. Bouazizi, R. Bargougui, A. Oueslati, R. Benslama, Effect of synthesis time on structural, optical and electrical properties of CuO nanoparticles synthesized by reflux condensation method, Adv. Mater. Lett. 6 (2) (2015) 158–164.

[55] L.D. Tijing, J.-S. Choi, S. Lee, S.-H. Kim, H.K. Shon, Recent progress of membrane distillation using electrospun nanofibrous membrane, J. Membr. Sci. 453 (2014) 435–462.

[56] Y. Xu, et al., In-situ silica nanoparticle assembly technique to develop an omniphobic membrane for durable membrane distillation, Desalination 499 (2021), 114832.

[57] T. Ni, J. Lin, L. Kong, S. Zhao, Omniphobic membranes for distillation: opportunities and challenges, Chin. Chem. Lett. 32 (11) (2021) 3298–3306.

[58] R. Zheng, Y. Chen, J. Wang, J. Song, X.-M. Li, T. He, Preparation of omniphobic PVDF membrane with hierarchical structure for treating saline oily wastewater using direct contact membrane distillation, J. Membr. Sci. 555 (2018) 197–205.

[59] S.R. Khan, B. Sharma, P.A. Chawla, R. Bhatia, Inductively coupled plasma optical emission spectrometry (ICP-OES): a powerful analytical technique for elemental analysis, Food Anal. Methods (2022) 1–23.

[60] S.H. Woo, J. Park, B.R. Min, Relationship between permeate flux and surface roughness of membranes with similar water contact angle values, Sep. Purif. Technol. 146 (2015) 187–191.

[61] J.A. Bush, et al., Prevention and management of silica scaling in membrane distillation using pH adjustment, J. Membr. Sci. 554 (2018) 366–377.

[62] C.F. Couto, M.C.S. Amaral, L.C. Lange, L.V. de Souza Santos, Effect of humic acid concentration on pharmaceutically active compounds (PhACs) rejection by direct contact membrane distillation (DCMD), Sep. Purif. Technol. 212 (2019) 920–928.

[63] L. Han, T. Xiao, Y.Z. Tan, A.G. Fane, J.W. Chew, Contaminant rejection in the presence of humic acid by membrane distillation for surface water treatment, J. Membr. Sci. 541 (2017) 291–299.

[64] L. Gazagnes, S. Cerneaux, M. Persin, E. Prouzet, A. Larbot, Desalination of sodium chloride solutions and seawater with hydrophobic ceramic membranes, Desalination 217 (1–3) (2007) 260–266.

[65] L.-H. Chen, et al., Omniphobic membranes for direct contact membrane distillation: effective deposition of zinc oxide nanoparticles, Desalination 428 (2018) 255–263.